Research

CrossMark
click for updates

Processes controlling surface, bottom and lateral melt of Arctic sea ice in a state of the art sea ice model

Michel Tsamados[1,2], Daniel Feltham[1], Alek Petty[3], David Schroeder[1] and Daniela Flocco[1]

[1]Centre for Polar Observation and Modelling, Department of Meteorology, University of Reading, Reading, UK
[2]Centre for Polar Observation and Modelling, Department of Earth Sciences, University College London, London, UK
[3]Earth System Science Interdisciplinary Center, University of Maryland, College Park, MD, USA

We present a modelling study of processes controlling the summer melt of the Arctic sea ice cover. We perform a sensitivity study and focus our interest on the thermodynamics at the ice–atmosphere and ice–ocean interfaces. We use the Los Alamos community sea ice model CICE, and additionally implement and test three new parametrization schemes: (i) a prognostic mixed layer; (ii) a three equation boundary condition for the salt and heat flux at the ice–ocean interface; and (iii) a new lateral melt parametrization. Recent additions to the CICE model are also tested, including explicit melt ponds, a form drag parametrization and a halodynamic brine drainage scheme. The various sea ice parametrizations tested in this sensitivity study introduce a wide spread in the simulated sea ice characteristics. For each simulation, the total melt is decomposed into its surface, bottom and lateral melt components to assess the processes driving melt and how this varies regionally and temporally. Because this study quantifies the relative importance of several processes in driving the summer melt of sea ice, this work can serve as a guide for future research priorities.

1. Introduction

The Arctic sea ice cover has undergone a rapid decrease in extent (e.g. [1]) and thickness [2–4] over recent

decades; transitioning from a predominantly multi-year ice pack to an increasingly seasonal ice pack (e.g. [5]). This decline has been accompanied by increases in sea ice drift [6,7] and deformation [8] over a similar time period. The drastic regime shift observed in recent years suggests that the sea ice models developed following the early field campaigns of the 1960s/1970s (Arctic ice dynamics joint experiment), and the 1990s (surface heat budget of the Arctic Ocean) need to be re-evaluated against current sea ice conditions [9]. Some of the assumptions in these early models have since been challenged, both in their thermodynamic [10,11] and dynamic [12,13] components. In this study, we seek to understand the processes controlling the summer melt of Arctic sea ice, and thus we focus our attention on the various thermodynamic parametrization schemes included in a state-of-the-art sea ice model.

Large regional and temporal variability in the sea ice state and the oceanic/atmospheric forcing provides a significant challenge when trying to assess the various processes that contribute to Arctic sea ice melt. In addition, *in situ* measurements that provide a decomposition of sea ice melt processes (top, bottom and lateral melt) are sparse [14,15]. Recently, Perovich *et al.* [16] quantified the relative importance of surface ice/snow melt and bottom ice melt using autonomous ice mass balance buoys deployed over more than 10 years (2000–2013) that drifted from the North Pole towards the Fram Strait. The study found surface and bottom melt to be of a similar magnitude on average, although both exhibited large inter-annual and regional variability. The study also demonstrated an almost doubling of bottom melt over the period 2008 to 2013 with respect to the period 2000–2005. Measurements of lateral melt are lacking and parametrizations of lateral melt in sea ice models are based on observations taken in the 1980s (e.g. [17] and references therein). The contribution to total Arctic sea ice melt from lateral melt is thought to be small in comparison to bottom and surface melt over high concentration areas, meaning its impact is mainly limited to the marginal ice zone. The increased areal coverage of the summertime marginal ice zone over recent years [18] could, however, be increasing the relative importance of lateral melt on a basin scale.

Sensitivity studies of one-dimensional models of sea ice have been used in the past to assess the relative importance of different processes in driving the sea ice response to a prescribed external forcing in the Arctic [19] and in the Antarctic [20]. These approaches are helpful in understanding the mean behaviour of the sea ice system but fail to capture the spatio-temporal complexity of the sea ice response and ignore feedbacks between the atmosphere, ice and ocean. At the other end of the complexity spectrum, ice–ocean (IO) coupled models [21] and fully coupled atmosphere–ice–ocean models [22–24], can resolve the regional and temporal sea ice response and feedback processes but are computationally expensive and often remain too simplified in representing the physics of sea ice. As a compromise between physical complexity and computational expense, we use a stand-alone sea ice model coupled to a prognostic ocean mixed layer (denoted ML hereafter) model to quantify the impact of various new physical processes on the sea ice system while retaining realistic regional information.

The total volume of sea ice within the Arctic basin is controlled by a balance between a thermodynamic (growth/melt) and a dynamic (ice import/export) contribution [25]. Locally, the sea ice thickness is controlled by the balance of heat conduction ($F_{condbot}$, $F_{condtop}$, see figure 1) and incoming fluxes (F_{ice}, F_s, see figure 1) at its upper and lower surfaces. As illustrated by simple one-dimensional models [19], the mean sea ice thickness (and by extension the total volume of ice) is sensitive to the external forcing (e.g. temperature, humidity, wind, incoming radiation, ocean heat flux) as well as to the parametrizations used to describe the sea ice thermodynamic processes (e.g. albedo scheme, lead opening, snow and ice thermal properties, treatment of the interfaces). In our stand-alone set-up, the external forcing is to a large degree constrained by the reanalysis. However, the use of a prognostic melt pond scheme [27] modifies the incoming shortwave radiation at the ice–atmosphere interface and the inclusion of the Petty *et al.* [26] prognostic ML model alters the basal IO flux and allows feedbacks between the ice and the ML. Therefore, even with prescribed boundary conditions and a stand-alone sea ice model, the heat budget of the Arctic sea ice (figure 2*a*) and ML (figure 2*b*) can be substantially modified by the choice of parametrization schemes used.
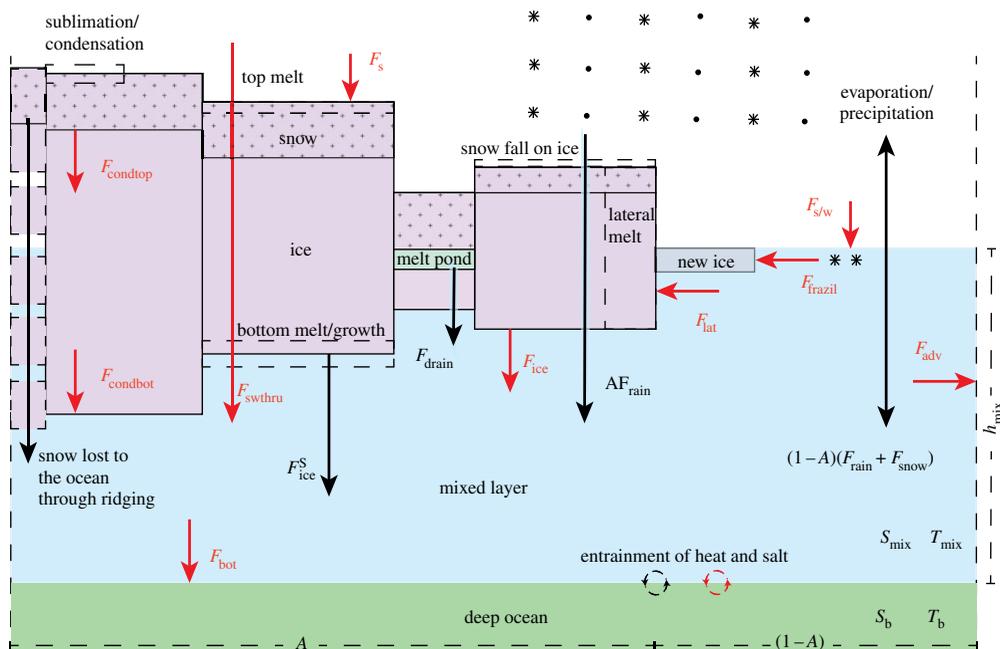
Figure 1. Schematic of the new prognostic ML module and of the other main thermodynamic processes included in CICE. The main heat fluxes are highlighted in red, while the main salt and freshwater fluxes are shown in black. Adapted from Petty *et al.* [26]. (Online version in colour.)
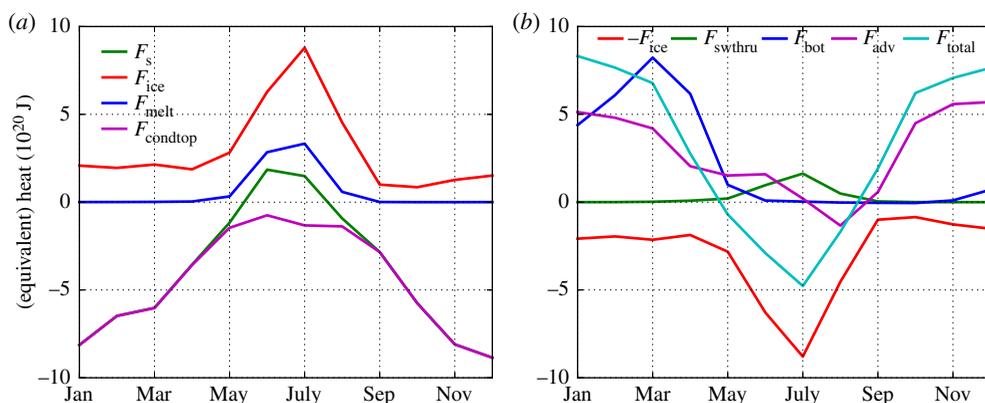

Figure 2. Climatology of the seasonal cycle of main components of the heat budget of the Arctic sea ice (*a*) and ML (*b*) over the period 1993–2012. All terms are expressed as an equivalent amount of heat entering the ice or ML (in Joules). (Online version in colour.)

To better understand the physical mechanisms affecting the large-scale retreat of the summer Arctic sea ice cover and the relative importance of lateral melt, basal melt and surface melt, we perform in this paper a sensitivity study of the summer sea ice state and melt to different sea ice physics parametrization schemes. The various model runs are analysed both in terms of their local response to a prescribed external forcing (melt rates, interface temperature, salinity and fluxes) as well as their basin scale ice state characteristics (total extent, area and volume).

The paper is structured as follows: §2 presents the model set-up, the sensitivity studies and the various physical processes assessed in this study; §3 discusses the model results, the impact on

the sea ice state characteristics, the ML properties and the relative importance of top, bottom and lateral melt in the model; and finally, a discussion and concluding remarks are given in §4.

2. Processes controlling ice melt in a sea ice model

(a) Choice of model configuration

We use v. 5.0.2 of the Los Alamos sea ice model, CICE, described in detail by Hunke *et al.* [28]. This state of the art sea ice model includes a large number of physical parametrization schemes that can be turned on or off by the user. Here, we briefly describe the schemes tested in this study.

The model uses multiple ice-thickness categories compatible with the ice thickness redistribution scheme of Lipscomb *et al.* [29]. We set the number of ice thicknesses to 5 and set the mean ridge height (a tuneable parameter) to $\mu_{rdg} = 4\,m^{1/2}$ [28]. We also use the default incremental remapping advection scheme of Lipscomb & Hunke [30].

In all model runs, we choose the elastic-anisotropic-plastic rheology described in Tsamados *et al.* [31]. This rheology is the default choice in our developmental branch of CICE and was shown to result in large regional differences in ice thickness with respect to the default elastic-viscous-plastic rheology of Hunke & Dukowicz [32]. We choose the ice strength formulation of Rothrock [33] and set the empirical parameter that accounts for frictional energy dissipation to $C_f = 17$.

CICE contains three explicit melt pond parametrizations [34] that are used in conjunction with the Delta-Eddington radiation scheme [35]. In all our runs, we use the physically based melt pond model of Flocco *et al.* [27], which simulates the evolution of melt ponds based on sea ice conditions and external forcing.

In this latest version of CICE, the vertical temperature and salinity profiles as well as the brine volume are calculated. We choose to resolve five ice layers and one snow layer vertically and compare model results between the fixed salinity profile parametrization of Bitz & Lipscomb [36] and the newly available mushy parametrization, in which the salinity within the ice can evolve in time (halodynamic model of Turner *et al.* [37]). The differences between the two models as well as the impact of both halodynamic components on the main sea ice characteristics are discussed in details in Turner & Hunke [38].

At the IO interface, we use the ocean heat flux formulation of Maykut & McPhee [39], $F_{ice} = \rho_w c_p \alpha_h u_* \Delta T$, ρ_w the water density, c_p the specific heat for seawater near freezing and α_h the Stanton number or sensible heat transfer coefficient. The friction velocity is calculated as $u_* = \sqrt{\tau_w/\rho_w}$, where τ_w is the IO drag (including form drag when calculated [40]). Finally, the temperature difference is taken as $\Delta T = T_{mix} - T_0$, with T_{mix} the ML temperature and T_0 the temperature at the IO interface. As a default in CICE, T_0 is chosen equal to the freezing temperature of water at the salinity of the ML, $T_0 = T_F(S_{mix})$.

In the default CICE set-up, both atmospheric (ANDC) and oceanic (ONDC) neutral drag coefficients are assumed constant in time and space. Following Tsamados *et al.* [40] and based on recent theoretical developments [41,42], the total neutral drag coefficients can now be estimated from properties of the ice cover such as ice concentration, vertical extent and area of the ridges, freeboard and floe draft, and size of floes and melt ponds. The new parametrization allows the drag coefficients to be coupled to the sea ice state and therefore to evolve spatially and temporally. For more detail on the implementation, we refer the reader to Tsamados *et al.* [40]. Note that in contrast to the earlier implementations of form drag in Tsamados *et al.* [40] or Hunke [43], we set the Stanton coefficient, α_h, to be proportional to the ONDC, C_{dw}.

As a default setting, we choose $\alpha_h = C_{dw}/2$, to be consistent with airborne measurements of neutral drag coefficients for heat and momentum over the Arctic sea ice (e.g. [44, fig. 6b]). Note that during the melt season when false bottoms (or any accumulation of low salinity water at the IO interface) cover a sufficiently large portion of the pack ice and limit bottom heat flux, reducing the parameter α_h can be qualitatively justified. As a simple representation of false bottoms, we therefore modify the IO heat transfer coefficient according to the melt pond concentration at the ice surface.

For lateral melt, we use the parametrization of Maykut & Perovich [45] and Steele [17] as implemented in CICE

$$\frac{\partial A}{\partial t} = -w_{\text{lat}}\frac{\pi}{\alpha L}A, \tag{2.1}$$

where A is the sea ice concentration, L is the typical floe diameter (set as a default in CICE to $L = 300$ m), α is a geometrical parameter, and w_{lat} is the lateral melting rate, parametrized as in Perovich [46], $w_{\text{lat}} = m_1 \Delta T^{m_2}$ ($m_1 = 1.6$, $m_2 = 1.36$).

We now describe the implementations that are currently unique to our developmental branch of CICE.

(b) Additional processes implemented in this study

(i) Prognostic mixed layer model in the Arctic

The default stand-alone configuration in CICE uses a fixed slab ocean ML with a prognostic ML temperature, T_{mix}, but a prescribed ML salinity from climatology, S_{mix}, and a constant ML depth, $h_{\text{mix}} = 20$ m. Here, we include the bulk ML model of Petty et al. [26] that was used to investigate shelf water formation around Antarctica. This simple prognostic ML model allows the temperature but also the salinity and the depth of the ML to evolve under the influence of surface and deep-ocean heat/salt fluxes. The model is based on the turbulent energy budget approach of Kraus & Turner [47], which assumes that temperature and salinity are uniform throughout the ML, and that there is a full balance in the sources and sinks of turbulent kinetic energy. The ML entrainment rate is then calculated by balancing the power needed to entrain water from below with the power provided by the wind and the surface buoyancy fluxes (see [26] for further details about this model choice).

At the surface, the ML receives a heat flux from the ice ($F_{\text{ice}} + F_{\text{swthru}}$, figure 1) and open-ocean fractions ($F_{s/w}$, figure 1) (all fluxes are positive downwards) and a salt flux calculated in CICE as a combination of ice/snow growth/melt (F^S_{ice}, figure 1) and precipitation and evaporation (F^S_{pe}, figure 1) (note that the rainfall and melt water on sea ice is assumed to percolate through the sea ice and enters the ML). In the winter as the ML deepens, heat and salt from the ocean below at the temperature, T_{b}, and salinity, S_{b}, are entrained in the ML (respectively, fluxes, F_{bot} and F^S_{bot}, figure 1), while in the summer as the ML shallows and leaves behind a layer of Winter Water, there are no heat or salt fluxes at the bottom of the ML. In our implementation, we introduce a minimum ML depth, $h^{\text{min}}_{\text{mix}}$ and assume that there are no heat and salt exchanges between the ML and the ocean below when the ML reaches this minimum.

We apply a slow ($\tau_{\text{r}} = 20$ days) temperature restoring of the ML temperature towards a monthly climatology of the 10 m depth reanalysis temperature taken from MYO-WP4-PUM-GLOBAL-REANALYSIS-PHYS-001-004 reanalysis [48] (hereafter noted MYO). This temperature restoring can be seen as a parametrization of the advection of heat in the upper ocean. The weak temperature restoring is consistent with model results from a coupled IO model [49] that found in the Arctic advection under the pack ice to be relatively small in comparison with surface heat fluxes. To represent oceanic heat flux convergence melting sea ice at the ice edge [50], we adopt a faster temperature restoring ($\tau_{\text{r}} = 2$ days) when $T_{\text{mix}} > T^{\text{MYO}}_{\text{mix}} + 0.2$. Note that the value of $0.2°$C is large enough to ensure that the fast restoring mainly occurs in the winter around the ice edge. This ad hoc method is equivalent to applying an additional heat flux to the ML, $F_{\text{adv}} = (T_{\text{mix}} - T^{\text{MYO}}_{\text{mix}})/(\tau_{\text{r}}\rho_{\text{w}}c_p h_{\text{mix}})$ (figure 1a). The fast temperature restoring is mostly important in controlling the winter sea ice extent (SIE), while the slow temperature restoring acts as a heat sink for the ML in the summer.

In addition to this temperature restoring, we use a slow (365 days) restoring to the sea surface salinity (SSS) in the ML. In our new prognostic ML set-up, the freezing temperature of the ML is updated to account for the modified salinity of the ML. As the ML shallows at the onset of melt, Winter Water is left behind in the deep ocean grid. The deep ocean salinity and temperature

are then slowly restored with a time scale of 1 year to a winter (1 January) climatology (1993–2010) from the MYO reanalysis. The ocean properties below the ML are therefore relaxed towards observed climatology, isolating the effect of surface forcing and allowing us to understand short-term (seasonal) variations in the ML.

(ii) Lateral melting and floe size distribution

We generalize the lateral melt parametrization of equation (2.1) to account for a power law distribution of floe sizes, in order to be consistent with observations (e.g. Herman [51] and references therein). In our new lateral melt parametrization scheme, the variable L in equation (2.1) represents the average floe size instead of representing a unique floe size as in the default lateral melt scheme.

For typical winter pack ice, $L \geq 100$ m [52] and lateral melting is negligible in comparison to bottom and surface melting [53]. In summer, the average floe size decreases and the relative importance of lateral melting to basal melting increases as the ratio of perimeter to area increases. Wave–ice interaction fractures the ice and leads to smaller floes in the marginal ice zone. The average floe size typically varies with the ice concentration and was parametrized in the marginal ice zone by Lüpkes et al. [42] to be:

$$L = L_{\min}\left(\frac{A_\star}{A_\star - A}\right)^\beta,$$ (2.2)

where $A_\star$ is introduced instead of the value 1 to avoid a singularity at $A = 1$, the exponent β is chosen in the range 0.2 to 1.4 ($\beta = 0.5$ in this study), and $L_{\min}$ is a characteristic minimal floe size ($L_{\min} = 8$ m in this study). Here, we have extended this parametrization to the entire ice cover, but note that in the case where $L \geq 100$ m, the contribution from lateral melting becomes negligible and the floe size parametrization becomes irrelevant to lateral melt.

In the appendix, we show that if one uses a power law floe size distribution, then the total lateral melt is reduced relatively to the situation with a unique floe size. Lateral melt is reduced by a factor $P_0(\zeta)$ applied to the right-hand side of equation (2.1),

$$\frac{\partial A}{\partial t} = -P_0(\zeta)w_{\mathrm{lat}}\frac{\pi}{\alpha L}A,$$ (2.3)

where ζ is the power exponent of the power law distribution $n_r(r)$, with $n_r(r)/\pi r^2$, being the number of floes of size r per unit area. Typical observed values of ζ are in the range 1–2 with the corresponding values of the attenuation pre-factor, respectively, $P_0(1) = 0$ and $P_0(2) = 0.75$. In this study, we choose $\zeta = 1.13$ and $P_0(1.13) = 0.2$. We should note that the choice of the exponent ζ is subjective and needs to be constrained further from observations.

(iii) Three equation boundary conditions

The Maykut & McPhee [39] formulation of the heat flux from the ocean into the ice, F_{ice} (§2a), depends on the interfacial temperature, T_0. As discussed in Schmidt et al. [54], the interfacial temperature can be chosen in models as (i) a constant freezing temperature of sea water (typically sea water at a salinity of 34 PSU); (ii) the freezing temperature of the ML (default option in CICE); or (iii) the freezing temperature, T_{f}, of the sea water directly below the sea ice with the interfacial salinity, S_0, that in the summer can be fresher than the water in the ML due to the freshwater fluxes associated with melting. In this last case, one must solve the following system of three equations described in Notz [55] and Mcphee [56]:

$$-F_{\mathrm{condbot}} + \rho_w c_p \alpha_h u_0^*(T_{\mathrm{mix}} - T_0) - q\dot{h}_0 = 0,$$ (2.4)

$$\alpha_s u_0^*(S_{\mathrm{mix}} - S_0) + \dot{h}_0(S_{\mathrm{ice}} - S_0) = 0$$ (2.5)

and

$$T_0 = T_{\mathrm{f}}(S_0) \simeq -mS_0,$$ (2.6)

where $F_{condbot}$ is the downward ice conductive heat flux at the basal surface, q is the enthalpy of new ice forming with the salinity and freezing temperature of the sea surface and $\dot{h}_0$ is the rate of ice growth at the IO interface. T_{mix} and S_{mix} are, respectively, the temperature and salinity of the ML. The exchange coefficients for salinity and heat are different under melting conditions, $\alpha_s = \alpha_h/50$ and under freezing conditions, $\alpha_s = \alpha_h$ [56].

Note that this is a new parametrization scheme included in CICE. We solve the system of equations (2.4)–(2.6) separately for each ice thickness category and save T_0, S_0 as well as all fluxes as output variables. Note that this parametrization scheme is only operational in CICE when the mushy layer parametrization of Turner *et al.* [37] is switched on.

(c) Reference model run and sensitivity model runs

We describe in this section our chosen reference run and model sensitivity runs. Our ambition is not to find an optimal model configuration but instead to test the impact of the model physics on a sufficiently realistic model configuration. The reference configuration follows largely from previous work by Tsamados *et al.* [40] and Schröder *et al.* [57] that included several recent model developments (§2a) and was able to demonstrate good agreement to the observed September SIE. In addition, our reference model configuration was chosen to reproduce reasonably well the main sea ice characteristics in the summer months, in particular the sea ice concentration in August that is often underestimated in models [58]. Because they are implemented in CICE for the first time, we focus in particular in our sensitivity study on the processes described in §2b.

In the reference run, *REF*, most model implementations described in §2a,b are switched on, namely the prognostic ML of Petty *et al.* [26]; the three equation boundary condition treatment of the IO interface; the mushy layer thermodynamic implementation of Turner *et al.* [37]; the form drag parametrization of Tsamados *et al.* [40]; a heat transfer coefficient proportional to the ONDC, $\alpha_h = C_{dw}/2$. On the other hand, the new lateral melt parametrization is not used.

In addition to the *REF* run, we perform a series of sensitivity runs. We adopt for each physical process a simple on–off approach where each additional model run contains a simple modification with respect to the *REF* run. The names and changes in these sensitivity runs are as follows. In *MLD_CST*, we use the default fixed depth slab ocean ML described in §2b; in *MLD_MIN_2M*, we set the minimum allowed ML depth to $h_{mix} = 2\,m$; in *NO_3EQTN*, we revert to the default boundary condition treatment with $T_0 = T_f(S_{mix})$ (§2b); in *NO_MUSHY*, we replace the mushy parametrization and flushing of Turner & Hunke [38] by the fixed salinity profile scheme of Bitz & Lipscomb [36] (§2a); *DBL_ALPHA_H*, *DBL_ALPHA_H / NO_3EQTN* and *DBL_ALPHA_H / NO_MUSHY* are the same as *REF*, *NO_3EQTN* and *NO_MUSHY* but with a doubling of α_h (§2a); in *NO_POND*, we artificially set the thickness of the melt ponds to zero; in *FALSE_BOTTOM* to simply model the impact of under ice fresh water accumulation on the bottom heat flux we double α_h where melt ponds cover less than 20% of the ice surface; in *NO_FORM_DRAG*, we switch off the Tsamados *et al.* [40] form drag parametrization (§2a); in *LAT_MELT*, we switch on the lateral melt parametrization described in §2b; finally, in *SST_TIME*, we restore the sea surface temperature (SST) to the time-dependent temperature of the MYO reanalysis surface ocean temperature over the period 1993–2010 (because the ocean reanalysis is limited to this period). All the sensitivity runs are summarized in table 1.

All simulations are run in stand-alone mode on a $1°$ tripolar (129×104) grid that covers the whole Arctic Ocean (note that the Hudson Bay and part of the Canadian Archipeleago are treated as land) with a horizontal grid resolution of around 50 km. Atmospheric forcing data are taken from the NCEP–NCAR reanalysis [59]: 6 hourly 10 m winds, 2 m temperatures and 2 m humidity, daily shortwave and longwave radiation as well as monthly snowfall and precipitation rates. SST and SSS are taken from the MYO reanalysis [48] to initialize the Arctic sea ice state. Climatological monthly means from Ferry *et al.* [48] are used for the ocean currents (depth of 10 m). Starting with an homogeneous sea ice with thickness of 2.5 m, a snow depth of 20 cm and a concentration of 100%, the reference model, *REF*, is spun up for 10 years (1980–1989) once. This configuration is

Table 1. Overview of all sensitivity runs.

description	name
REF	reference run: prognostic ML [26][a], low heat transfer coefficient $\alpha_h = C_{dw}/2$, form drag [40], fixed floe size ($L = 300$ m), thermodynamics and flushing of Turner & Hunke [38][a], three equation boundary condition[c]
MLD_CST	as *REF* but default prescribed ML ($h_{mix} = 20$ m)[b]
MLD_MIN_2M	as *REF* but $h_{mix}^{min} = 2$ m instead of default $h_{mix}^{min} = 10$ m[a]
NO_3EQTN	as *REF* but default boundary condition $T_0 = T_f(S_{mix})$[c]
NO_MUSHY	as *REF* but thermodynamics of Bitz & Lipscomb [36] and default boundary condition $T_0 = T_f(S_{mix})$[c]
DBL_ALPHA_H	as *REF* but $\alpha_h = C_{dw}$[c]
DBL_ALPHA_H / NO_3EQTN	as *REF* but doubling heat transfer coefficient $\alpha_h = C_{dw}$ and default boundary condition $T_0 = T_f(S_{mix})$[c]
DBL_ALPHA_H / NO_MUSHY	as *REF* but doubling heat transfer coefficient $\alpha_h = C_{dw}$, thermodynamics of Bitz & Lipscomb [36], and default boundary condition $T_0 = T_f(S_{mix})$[c]
NO_POND	as *REF* but melt ponds area and thickness set to zero[d]
FALSE_BOTTOM	as *REF* but Thermodynamics of Bitz & Lipscomb [36], $T_0 = T_f(S_{mix})$[c], $\alpha_h = C_{dw}$ but $\alpha_h = C_{dw}/2$ if $A_p \geq 20\%$ in *ad hoc* description of false bottoms[d]
NO_FORM_DRAG	as *REF* but $C_{da} = 1.2 \times 10^{-3}$, $C_{dw} = 6.09 \times 10^{-3}$ SKIN set-up of Tsamados *et al.* [40][e]
LAT_MELT	as *REF* but Power law FSD with average floe size $L(A)$[f]
SST_TIME	as *REF* but Temperature restoring towards a time-dependent MYO SST[a]
SFFT14	set-up of Schröder *et al.* [57] (fixed ML depth, $\alpha_h = 0.006$)

[a]See §2b. All other model runs contain a single modification with respect to *REF*.
[b]See §2a.
[c]See §2b, note that BF stands here for bottom flux.
[d]See §2a, note that FB stands here for false bottom.
[e]See §2a, note that FD stands here for form drag.
[f]See §2b.

used as initial condition for all the simulation runs described in table 1 that are then run for a period of 24 years (1990–2013).

3. Results of a sensitivity study

(a) Relative importance of top, bottom and lateral melt

In this section, we describe the impact of the various parametrization schemes on the summer Arctic sea ice–ML state. Figure 3 shows the mean seasonal and inter-annual ML temperature T_{mix} (figure 3a,b), ML salinity S_{mix} (figure 3e,f) and ML depth h_{mix} (figure 3i,j) for each model simulation. To decompose the thermodynamic response of each model simulation and to quantify the relative importance of top, bottom and lateral melt, figure 3 shows the mean seasonal and inter-annual surface melt rate (figure 3c,d), bottom melt rate (figure 3g,h) and lateral melt rate (figure 3k,l).

Looking first at the mean upper ocean characteristics, we see that the seasonal cycle of h_{mix} is important in controlling the temperature and salinity of the ML. From a simple heat and salt conservation argument (eqs 14 and 15 in Petty *et al.* [26]), the shallowing of the ML in the summer season results in an increase of the average T_{mix} (figure 3a), from an average maximum in July of
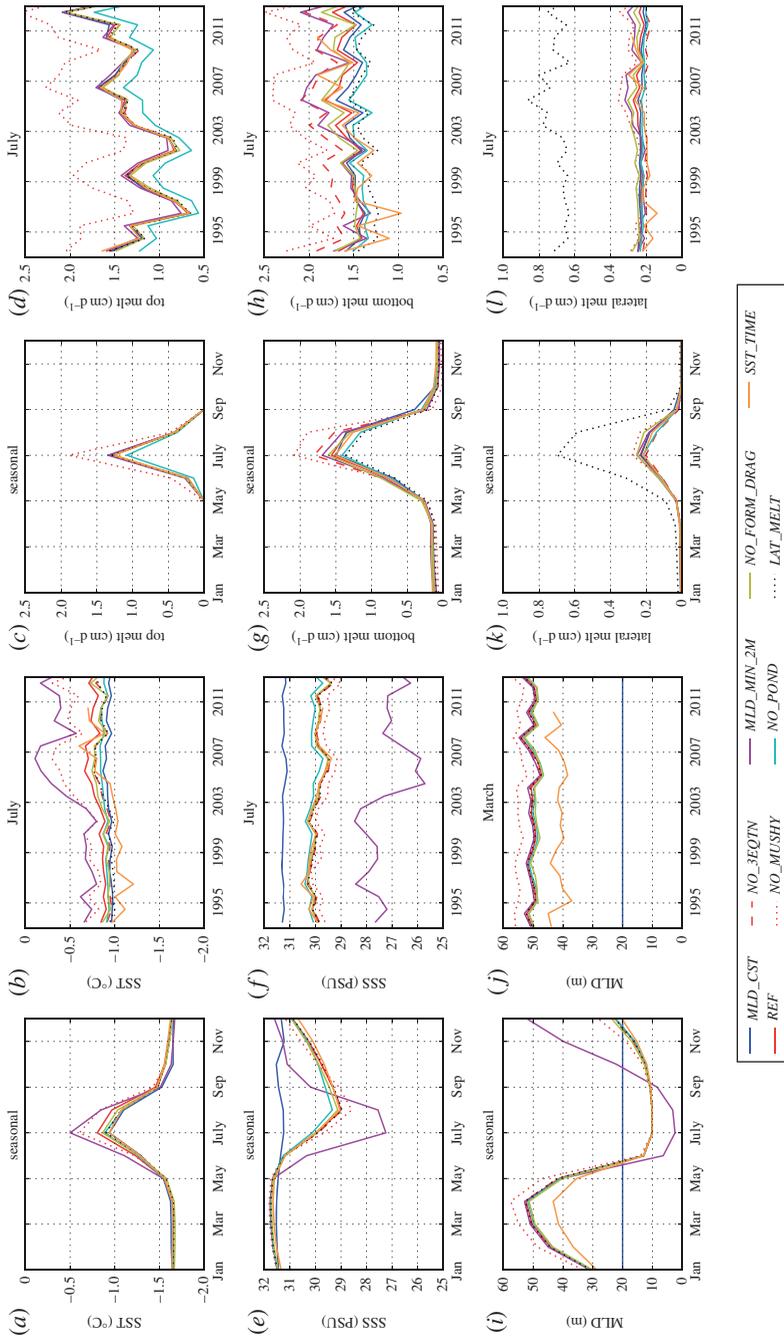
Figure 3. Impact of the sensitivity model runs on SST (*a,b*), SSS (*e,f*), ML depth (*i,j*), top melt (*c,d*), bottom melt (*g,h*) and lateral melt (*k,l*). Figures on the first and third columns show the seasonal climatology calculated over the period 1993–2012, while columns 2 and 4 show time series for July (except (*j*) that shows the MLD in March). The colour code is the same as in figure 2. (Online version in colour.)

~$-1.0°C$ in *MLD_CST* to ~$-0.8°C$ in *REF* and ~$-0.5°C$ in *MLD_MIN_2M* and a reduction of the average minimum SSS in July (figure 3*e*) from ~31.3 PSU to ~29 PSU and ~27.4 PSU. In addition to the seasonal dependence, the ML appears to be warming (figure 3*b*) and freshening (figure 3*f*) over the last two decades in July and this trend is stronger for the shallower summer ML in *MLD_MIN_2M*. Interestingly, despite having a thicker h_{mix}, *NO_MUSHY* displays very similar T_{mix} characteristics as in *MLD_MIN_2M*. This reflects the additional incoming solar radiation in this model run that was shown by Turner & Hunke [38] to be related to the reduced flushing rate in the Bitz & Lipscomb [36] parametrization resulting in a larger pond area fraction and a lower albedo. The summer T_{mix} climatology in *NO_3EQTN*, *NO_FORM_DRAG*, *NO_POND* and *SST_TIME* is lower than *REF* by approximately 0.1°C. Note also that in *SST_TIME*, there is a strong warming trend of the ML and the inter-annual variability of T_{mix} is much larger than in *REF*. This points to the importance of the oceanic temperature restoring scheme used in a stand-alone setting. These variations in the mean ML characteristics can help us explain the differing bottom and lateral melt rates from each simulation as discussed next.

The bottom and lateral heat fluxes scale, respectively, with ΔT and ΔT^{m_2} ($\Delta T = T_{mix} - T_0$, see §2*c*). Intuitively, one might therefore expect a higher summer T_{mix} will contribute to an increase in the bottom and lateral heat flux. However, a fresher ML results in an increased freezing temperature at the IO interface (here we assume $T_0 = T_F(S_{mix})$) which will reduce the bottom and lateral heat flux. Comparing *MLD_CST* and *REF* in figure 3*g,h*, we can see that despite the higher T_{mix} in the *REF* simulation, the impact on the average local bottom melt is negligible. In the *MLD_MIN_2M* and *NO_MUSHY* simulations, however, the increase in T_{mix} compared with *REF* appears sufficient to cause a significant increase in the bottom and lateral melt (figure 3*h,l*). Finally, the *NO_3EQTN* simulation demonstrates the insulating effect caused by switching on the three equation boundary conditions. Indeed, despite the higher T_{mix} throughout summer in the *REF* simulation, the bottom melt rate is significantly higher on average for *NO_3EQTN*. This can only be explained by the larger interfacial temperature in *REF* (not shown) that, in contrast to *NO_3EQTN*, is taken as the freezing temperature of the fresher water directly below the sea ice (equations (2.4)–(2.6)).

The mean seasonal (figure 3*c,g,k*) and annual time series (figure 3*d,h,l*) of the basin average surface, bottom and lateral melt rates show that the bottom melt is the strongest contributor to the total melt (up to ~$1.5\,\mathrm{cm\,d^{-1}}$ in July for *REF*). The top melt is the second strongest contribution (up to ~$1.25\,\mathrm{cm\,d^{-1}}$ in July for *REF*) and, as expected, is largely insensitive to modifications to the ML. Except in the case of the floe size-dependent lateral melt parametrization, *LAT_MELT*, the contribution from lateral melt is on average small (up to ~$0.25\,\mathrm{cm\,d^{-1}}$ in July for *REF*). For the *REF* simulation in July, surface melt shows the highest inter-annual variability, with a standard deviation of $0.41\,\mathrm{cm\,d^{-1}}$ (figure 3*d*), compared with $0.29\,\mathrm{cm\,d^{-1}}$ for bottom melt (figure 3*h*) and $0.06\,\mathrm{cm\,d^{-1}}$ for lateral melt (figure 3*l*). These results suggest that in our model implementation, inter-annual variability of the summer sea ice characteristics (area, extent and volume) will be dominated by the surface melt processes. This could explain why the inclusion of a realistic description of surface melt ponds in CICE results in significant skill in reproducing and forecasting the September SIE [57]. Note also that the lower inter-annual variability in *REF* ($0.29\,\mathrm{cm\,d^{-1}}$) compared with *SST_TIME* ($0.36\,\mathrm{cm\,d^{-1}}$) could indicate that the simulations without temperature restoring to a time-dependent reanalysis might underestimate the true variability of the upper ocean temperature and salinity.

Figure 4 decomposes the changes in the total volume of ice into its various thermodynamic components during ice growth (congelation growth, frazil ice formation and snow ice formation) and ice melt (surface melt, bottom melt and lateral melt). Figure 4 shows that the mean annual ice growth is dominated in all sensitivity simulations by congelation growth (+9500 km^3 in *REF*), followed by frazil ice formation (+4100 km^3 in *REF*), and snow ice formation (+800 km^3 in *REF*). The mean annual ice melt is dominated by bottom melt ($-10\,000\,\mathrm{km}^3$ in *REF*), followed by surface melt ($-3200\,\mathrm{km}^3$ in *REF*) and lateral melt ($-1200\,\mathrm{km}^3$ in *REF*). In all the simulations, the total annual ice melt and growth largely cancel each other out over the full annual cycle, leaving only a small negative term associated with the expected ice volume decline over the 1993–2010
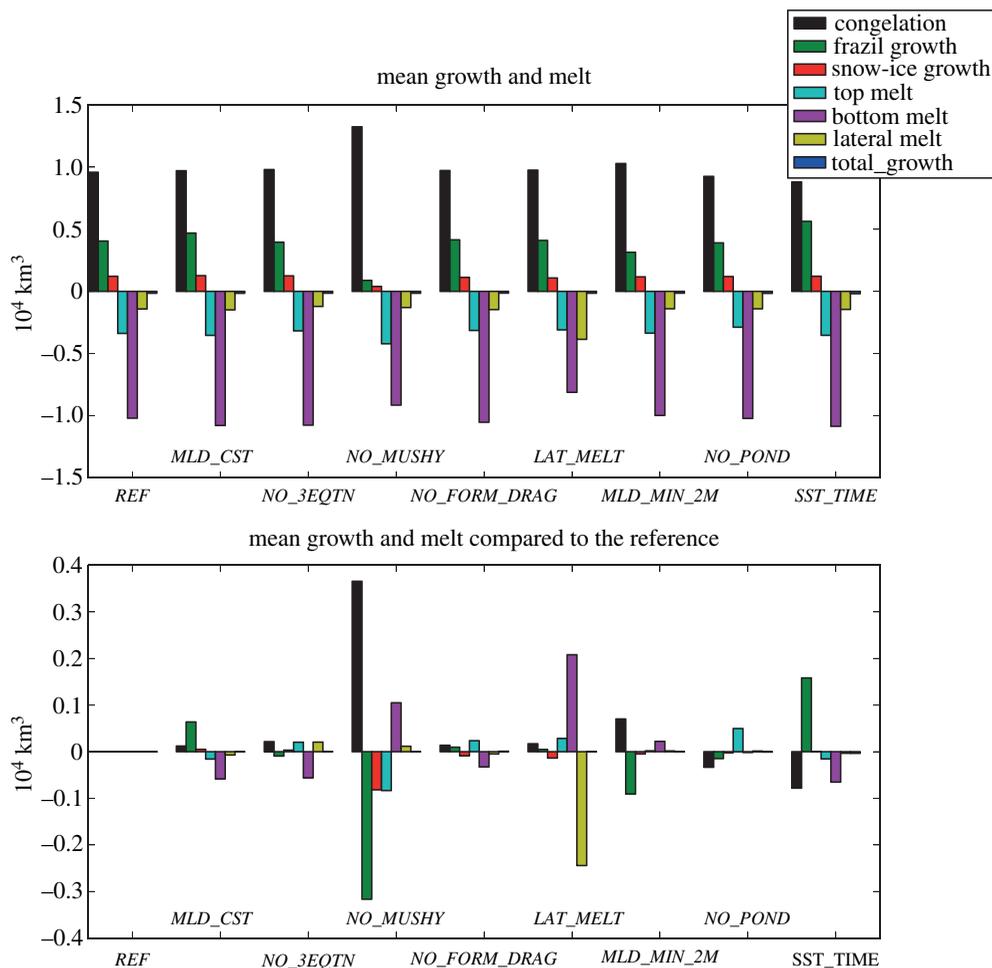
Figure 4. Mean annual volume of ice gained or lost through thermodynamic processes associated with our collection of models between 1993 and 2010. The incremental differences from the reference run *REF* volume for each process are shown in the second plot; e.g. positive melt terms indicate increased ice volume due to decreased melting, relative to *REF*. Note the differing scales in the two plots. (Online version in colour.)

period. The differences in the mean total sea ice volume (SIV) across all simulations occur in a transient period of up to 5 years from 1990 to 1994 (not shown). Three simulations stand out in figure 4, *NO_MUSHY*, *LAT_MELT* and *SST_TIME*. Relative to *REF*, *NO_MUSHY* shows an overall increase in congelation growth ($+3750 \, \text{km}^3$) and a reduction in surface melt ($-900 \, \text{km}^3$) and lateral melt ($-200 \, \text{km}^3$), compensated by a decrease in frazil ice formation ($-3100 \, \text{km}^3$) and an increase in snow ice formation ($+850 \, \text{km}^3$) and bottom melt ($+950 \, \text{km}^3$). The increase in lateral melt in *LAT_MELT* ($-2500 \, \text{km}^3$) is largely compensated by a reduction in bottom melt ($+2200 \, \text{km}^3$) reflecting the fact that the heat available in the ML to melt the ice from below is divided between lateral and bottom melt. In *SST_TIME*, a large increase in frazil ice formation is compensated by less congelation growth and increased bottom melt. These compensating effects are examples of the negative feedback processes that take place during the thermodynamic cycle of sea ice.

Decomposing the total ice melt shows that bottom melt accounts for more than two-thirds of the total ice melt, top melt accounts for almost a third of the total and lateral melt contributes less than 10%. Looking at the ice melt across individual months (not shown) shows that a significant

fraction of the total bottom melt occurs outside the summer melt season (from September to April), featuring monthly ice melt volumes of -2000 to $-5000\,\mathrm{km}^3$. Over the same monthly time period, the contribution to the total melt from surface and lateral melt is small. Looking at maps of ice melt (similar to figure 6) for the September to April months (not shown) demonstrates that this 'winter' bottom melt contribution occurs mainly around the ice edge, driven by warm southern Atlantic and Pacific waters. In the *REF* simulation, the monthly (inter-annual) mean ice melt in June, July and August is -6000, $-28\,000$ and $-5000\,\mathrm{km}^3$ for surface melt, $-22\,000$, $-38\,000$ and $-22\,000\,\mathrm{km}^3$ for bottom melt and -4000, -5000 and $-3000\,\mathrm{km}^3$ for lateral melt.

We now look at the spatial pattern of the surface (figure 5), bottom (figure 6) and lateral (figure 7) melt for each simulation for July (the maximum melt month). In these figures, absolute melt rates are shown for *REF*, while relative values are shown for all other model runs. Looking first at the absolute values of the melt rates in *REF*, we see that the mean July surface melt rate is high ($\sim 1.5\,\mathrm{cm\,d}^{-1}$) over most of the Arctic basin and is low (less than $0.5\,\mathrm{cm\,d}^{-1}$) over the Fram Strait, the ice edge and the region of thicker ice north of Greenland and the Canadian Archipelago. Note that the regions of increased surface melt correspond to regions of larger than average pond coverage (not shown). The bottom and lateral melt rates are higher (more than or equal to $1.5\,\mathrm{cm\,d}^{-1}$ and more than or equal to $0.25\,\mathrm{cm\,d}^{-1}$, respectively) in regions of low concentration ($A < 80\%$), where solar radiation can penetrate the upper ocean and increase the ML temperature.

Figure 5 shows that model runs using the Bitz & Lipscomb [36] parametrization for salinity and flushing (*NO_MUSHY*, *DBL_ALPHA_H* / *NO_MUSHY* and *FALSE_BOTTOM*) result in a large increase in surface melt ($+0.25$ to $+0.5\,\mathrm{cm\,d}^{-1}$). This is the result of a slower flushing of melt ponds resulting in a lower surface albedo and higher incoming solar radiation. This in turn leads to increased heat transfer to the ML and an increase bottom ($+0.25$ to $+1.0\,\mathrm{cm\,d}^{-1}$) and lateral melt rate (up to $+0.1\,\mathrm{cm\,d}^{-1}$) over most of the Arctic Ocean. The similarity in the spatial patterns of bottom and lateral in *NO_MUSHY* and *FALSE_BOTTOM* demonstrates that reducing the heat transfer coefficient only in those locations that present large coverage of ponds (pond area larger than 20%) is sufficient to significantly reduce the oceanic melt. This hints to the potentially important role of under ice melt ponds and false bottom formation in controlling the sea ice state.

In *LAT_MELT*, we observe a large increase of lateral melt over the ice edge (more than or equal to $0.5\,\mathrm{cm\,d}^{-1}$) that is accompanied by a reduction in bottom melt (less than or equal to $-0.5\,\mathrm{cm\,d}^{-1}$). This highlights that if more heat is used to melt the ice laterally, less heat is available for bottom melt. Figure 5 shows a decrease in *NO_FORM_DRAG* of bottom melt under heavily ridged ice north of Greenland and the Canadian Archipelago (less than or equal to $-0.25\,\mathrm{cm\,d}^{-1}$) that we attribute to a reduction in *NO_FORM_DRAG* with respect to *REF* of the oceanic drag coefficient, C_{dw}, and hence a reduction in the heat transfer coefficient, $\alpha_\mathrm{h} = C_{dw}/2$.

Other interesting spatial features include the near identical spatial patterns of bottom and lateral melt rates in *MLD_CST* and *NO_POND* which mirror the melt rates observed in *MLD_MIN_2M*. We also note that turning off the three equation boundary conditions in the *NO_3EQTN* simulation results in an increased bottom and lateral melt in the marginal ice zone. In order to fully understand the pattern of the melt rates discussed above, we now look at the impact on the main sea ice and ML characteristics.

(b) Regional sea ice and mixed layer patterns

The ice cover is a complex heterogeneous system and in this section we assess how different regions respond to the different physical parametrization schemes. For all model simulations (described in table 1), we calculate for each model grid cell a climatology (over the period 1993–2013) of sea ice concentration (A), sea ice thickness (H), ML temperature (T_mix) and ML salinity (S_mix). As discussed in the Introduction, the main focus of this study is in understanding the sensitivity of sea ice melt to various sea ice physics parametrization. Nevertheless, our reference run was chosen to agree qualitatively with ice concentration data obtained from the Special Sensor Microwave Imager (SSM/I) passive microwave radiometer and with ice thickness from the Pan-Arctic Ice Ocean Modeling and Assimilation System (PIOMAS).
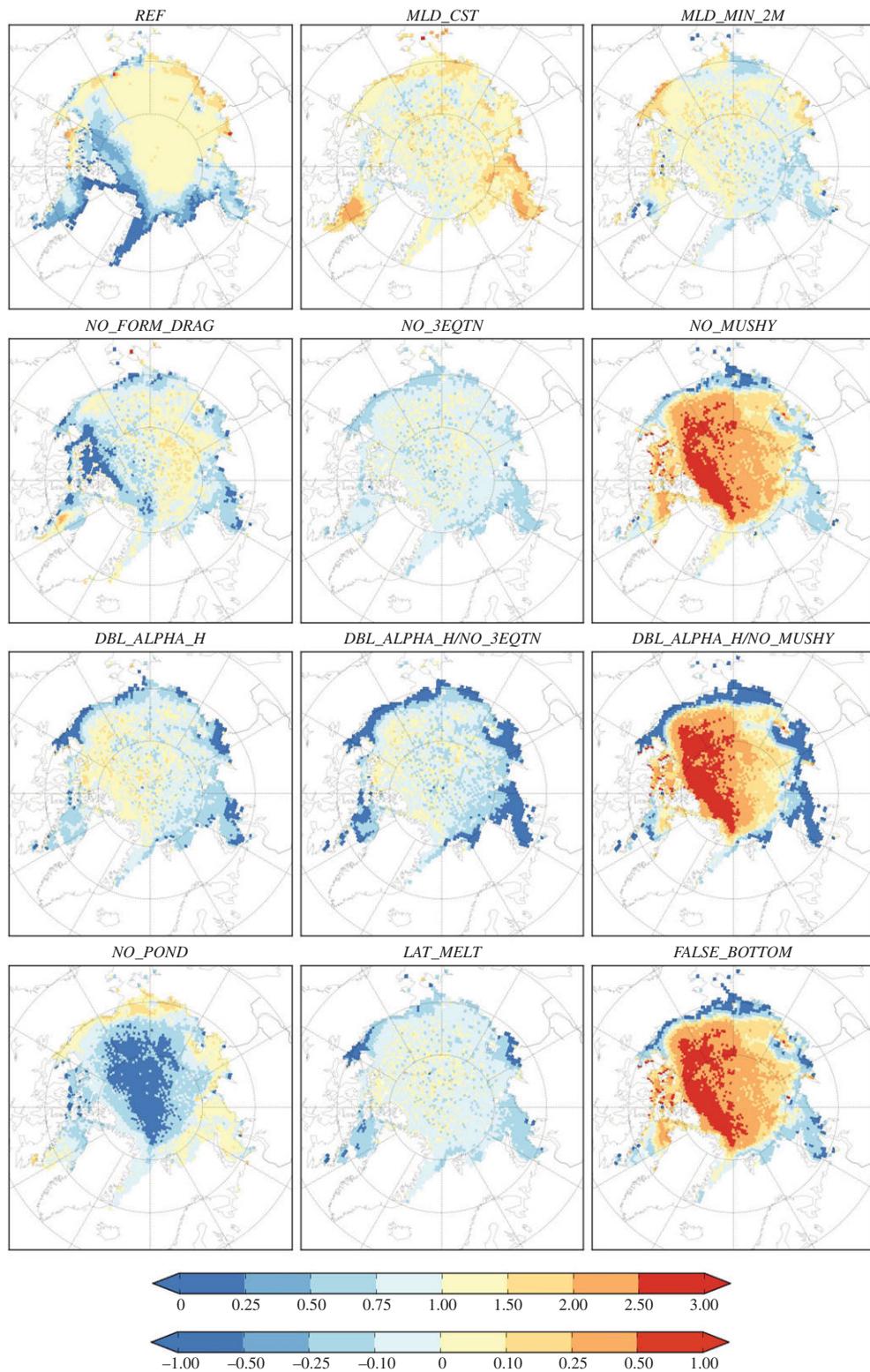
Figure 5. Maps of the climatology of the average July top melt over the period 1994–2013 for all sensitivity runs. Note that the map for the *REF* model run is given in absolute melt rate values (in cm d^{-1}, top colour bar), while all other model runs are given as difference in melt rate with respect to *REF* (in cm d^{-1}, bottom colour bar). (Online version in colour.)
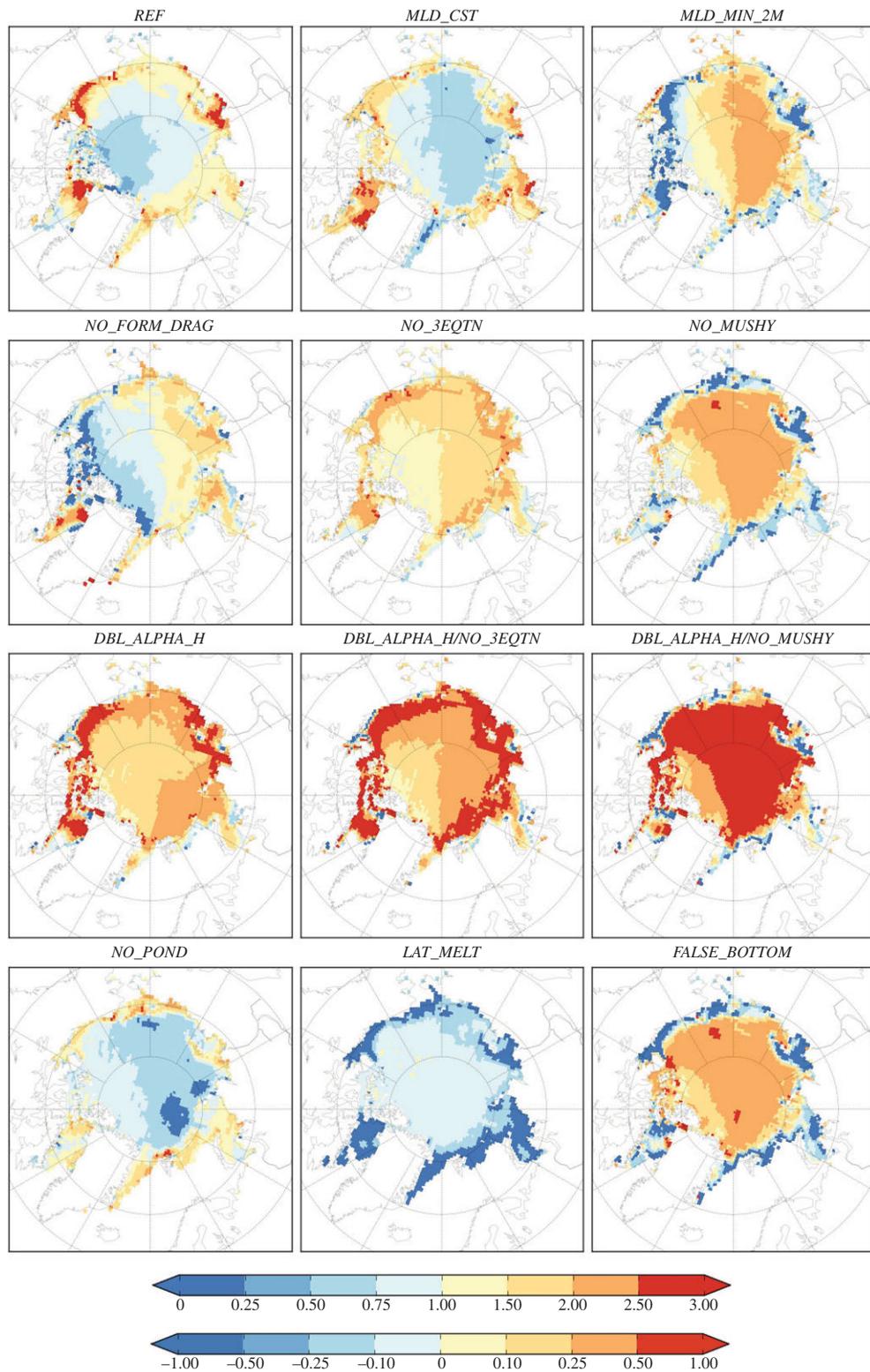
Figure 6. Maps of the climatology of the average July bottom melt over the period 1994–2013 for all sensitivity runs. Note that the map for the *REF* model run is given in absolute melt rate values (in cm d^{-1}, top colour bar), while all other model runs are given as difference in melt rate with respect to *REF* (in cm d^{-1}, bottom colour bar). (Online version in colour.)
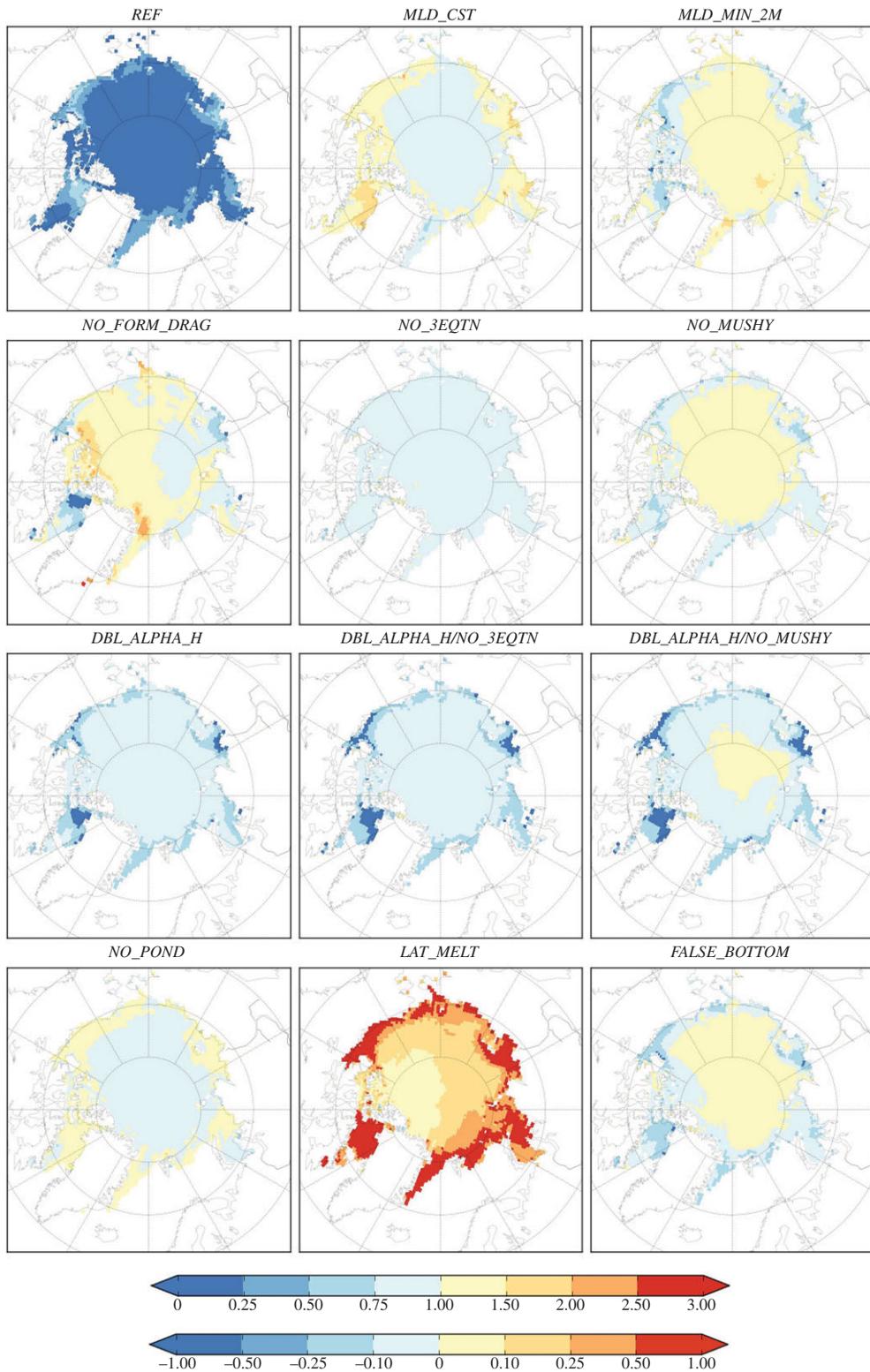
15

rsta.royalsocietypublishing.org Phil. Trans. R. Soc. A **373**: 20140167

Figure 7. Maps of the climatology of the average July lateral melt over the period 1994–2013 for all sensitivity runs. Note that the map for the *REF* model run is given in absolute melt rate values (in cm d^{-1}, top colour bar), while all other model runs are given as difference in melt rate with respect to *REF* (in cm d^{-1}, bottom colour bar). (Online version in colour.)

Comparing h_{mix} from Ice Tethered Profilers (ITP) measurements (2004–2013) and the MYO reanalysis, we find that the simulations presented in this study featuring only a simple prognostic ML model reproduce also qualitatively the shallow and stable ML observed across the Arctic (see also Peralta-Ferriz et al. [60]). In the summer, the REF simulation and the MYO reanalysis show a shallower ML depth than the ITP measurements, including a minimum depth of $h_{mix} \sim 10\,m$ over the entire Arctic Ocean. The REF simulation ML depths agree with the ITP measurements in the Beaufort Sea but underestimate the ML depths in the pack ice north of Greenland. Similar maps of the ML temperature (T_{mix}) and salinity (S_{mix}) (not shown) illustrate the tendency of the REF simulation to overestimate (both against ITP and MYO) the heating of the ML in August, which in turn results in additional melt and a lower S_{mix}.

In figures 8–11, we show maps of the main sea ice and ML characteristics. We show the absolute values for the reference REF simulation and the relative values with respect to REF for all other model simulations. We have computed these maps for all months but choose here to only show August. This choice is motivated first by the fact that August has the largest differences between the different sensitivity model runs in our study and also because August sea ice concentration is often underestimated in current sea ice models [58].

Comparing first REF, MLD_CST and MLD_MIN_2M, we see that switching off the prognostic ML results in a large increase in ice concentration (A > +10%, figure 8) and decrease in the ML temperature ($T_{mix} < -0.4°C$, figure 10) over most of the eastern Arctic Ocean (where $A < 80\%$, figure 8). Reducing the value of the minimum ML depth (to $h_{mix} = 2\,m$) has the opposite effect and results in a large decrease in concentration (A < −10%, figure 8) and increase in the ML temperature ($T_{mix} > +0.4°C$) over the same region. The impact on ice thickness is more diffuse, with a homogeneous increase in the mean ice thickness (+10 cm–25 cm, figure 9) over most of the Arctic basin for MLD_CST and a corresponding increase in the ML salinity (more than +2 PSU, figure 11). MLD_MIN_2M shows a decrease in ice thickness (−50 to −100 cm) over a similar region to MLD_CST and a corresponding decrease of the ML salinity (less than −2 PSU). This indicates that to a leading order the ML temperature tends to evolve with sea ice concentration (due to modified incoming solar radiation), while the ML salinity evolves with ice thickness (due to salt exchanges during ice melt/growth). Note that these results hold also in July and throughout the summer season (not shown).

We now turn to REF, NO_3EQTN and NO_MUSHY (results for DBL_ALPHA_H, DBL_ALPHA_H / NO_3EQTN and DBL_ALPHA_H / NO_MUSHY are qualitatively similar) to quantify the impact of the sea ice salinity dynamics, flushing and three equation boundary condition on the sea ice and ML. Because of the larger incoming solar radiation associated with the default halodynamic model of Bitz & Lipscomb [36] and the default CICE flushing parametrization, sea ice concentration is reduced in NO_MUSHY with respect to REF by more than 10%, sea ice thickness is reduced by more than 1 m, T_{mix} is higher by more than 0.4°C, and S_{mix} is lower by 0.5–1 PSU over most of the Arctic Ocean. Note that FALSE_BOTTOM, the simulation that uses the same Bitz & Lipscomb [36] parametrization has a similar low sea ice state bias. Comparing REF and NO_3EQTN, we see that the differences are smaller ($\Delta A \sim -5\%$, $\Delta H \sim -20\,cm$, $\Delta T_{mix} \sim +0.3°C$ and $\Delta S_{mix} \sim 0$ PSU), the impact is localized over the marginal ice zone and happens almost exclusively in the summer season (June and July not shown). This is consistent with the larger melt rate in this region in NO_3EQTN and reflects the fact the three-equation boundary condition is most effective where there is a source of fresh melted water at the IO interface, hence lowering the interfacial salinity, S_0, and reducing the bottom heat flux (see equations (2.4)–(2.6) in §2b).

The impact of switching off the form drag parametrization of Tsamados et al. [40] in NO_FORM_DRAG is spatially bi-modal; increasing the summer concentration (marginally), ice thickness ($\Delta H \sim +1\,m$) and ML salinity ($\Delta S_{mix} \sim 1$ PSU) in the heavily ridged regions north of Greenland and the Canadian Archipelago, and decreasing the ice concentration ($\Delta A \sim -10\%$) and ice thickness ($\Delta H \sim -25\,cm$) while increasing the ML temperature ($\Delta T_{mix} \sim +0.3°C$) over the Russian continental shelves. As discussed in §3a, these differences can be largely explained by increased (reduced) interfacial heat fluxes due to the higher (lower) than average atmospheric
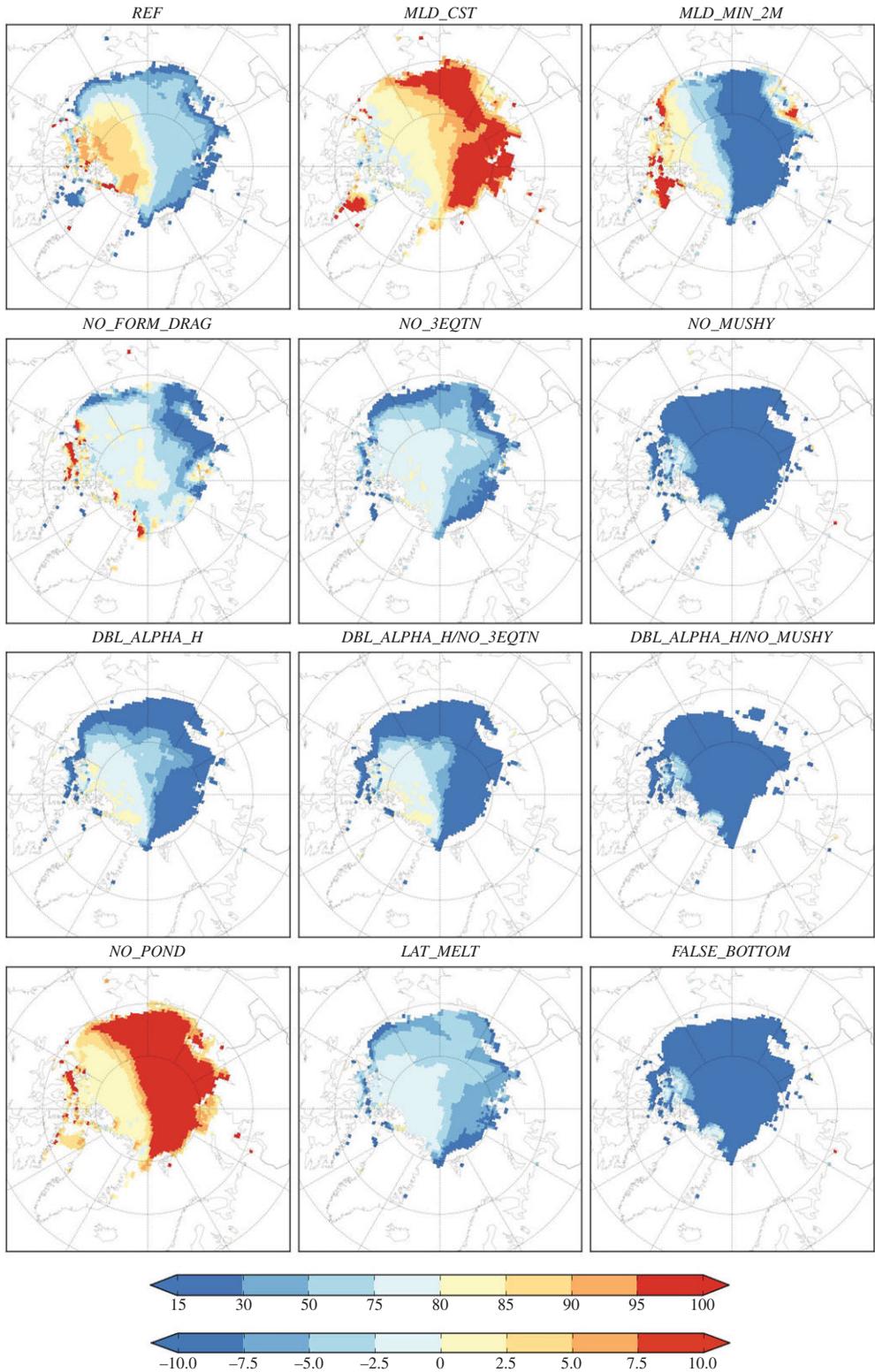
Figure 8. August sea ice concentration climatology maps over the period 1994–2013 for all sensitivity runs. Note that the map for the *REF* model run is given in absolute concentration values (in %, top colour bar), while all other model runs are given as difference in concentration with respect to *REF* (in %, bottom colour bar). (Online version in colour.)
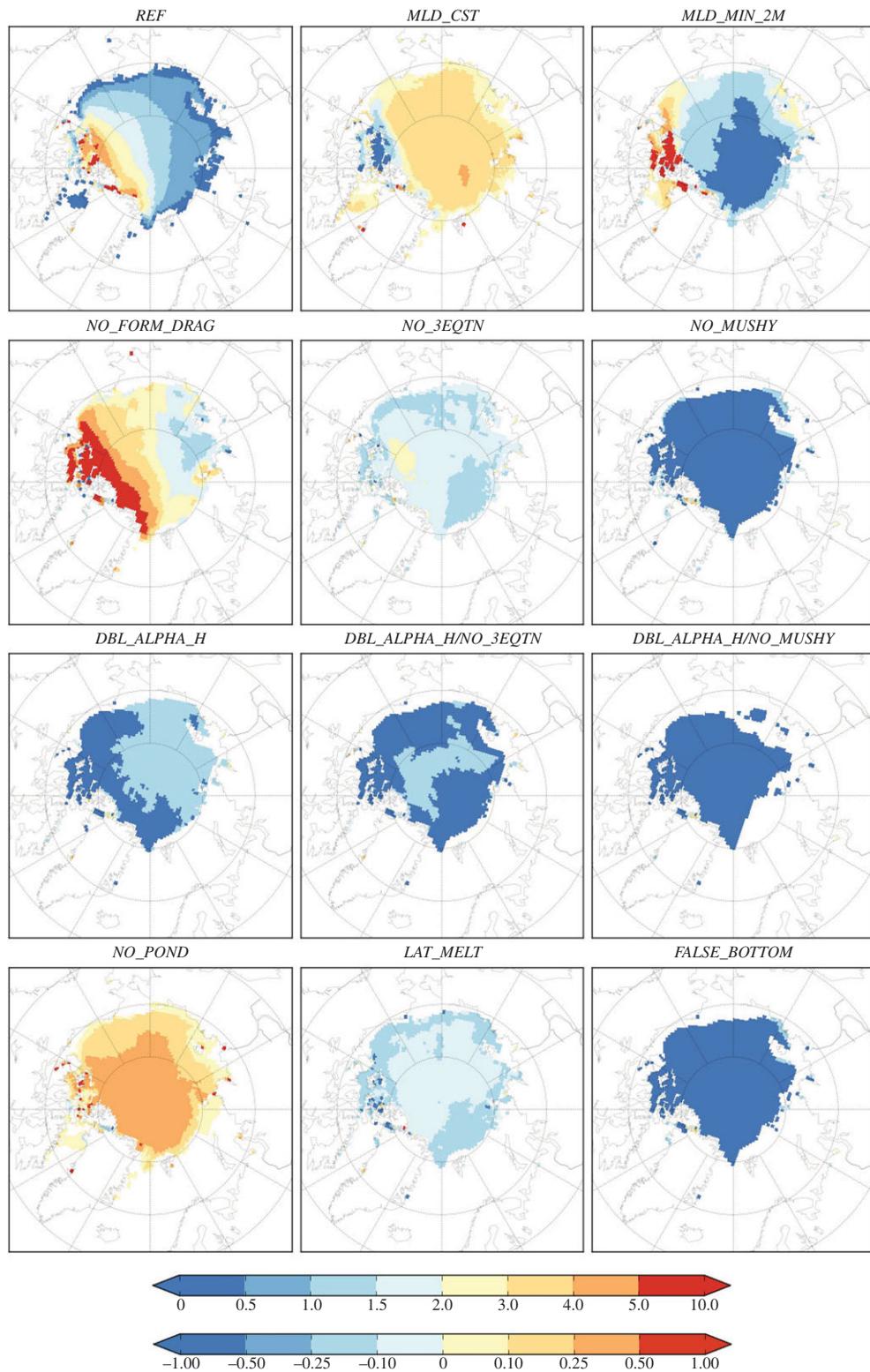
18

rsta.royalsocietypublishing.org *Phil. Trans. R. Soc. A* **373**: 20140167

Figure 9. August sea ice thickness climatology maps over the period 1994–2013 for all sensitivity runs. Note that the map for the *REF* model run is given in absolute thickness values (metres, in top colour bar), while all other model runs are given as difference in thickness with respect to *REF* (metres, in bottom colour bar). (Online version in colour.)
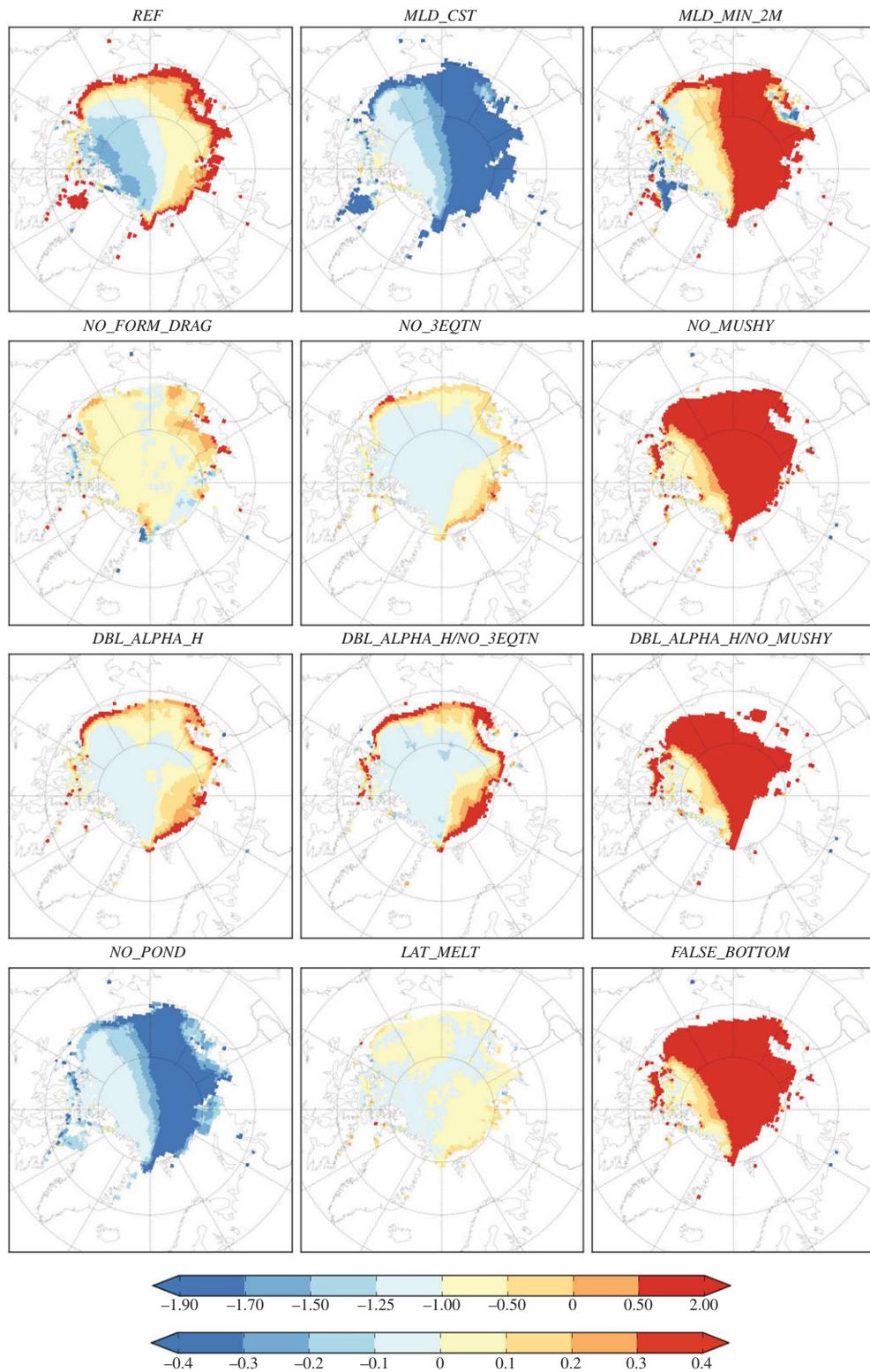
19

rsta.royalsocietypublishing.org Phil. Trans. R. Soc. A **373**: 20140167

Figure 10. August ML temperature climatology maps over the period 1994–2013 for all sensitivity runs. Note that the map for the *REF* model run is given in absolute temperature values (°C, in top colour bar), while all other model runs are given in as difference in temperature with respect to *REF* (°C, bottom colour bar). (Online version in colour.)
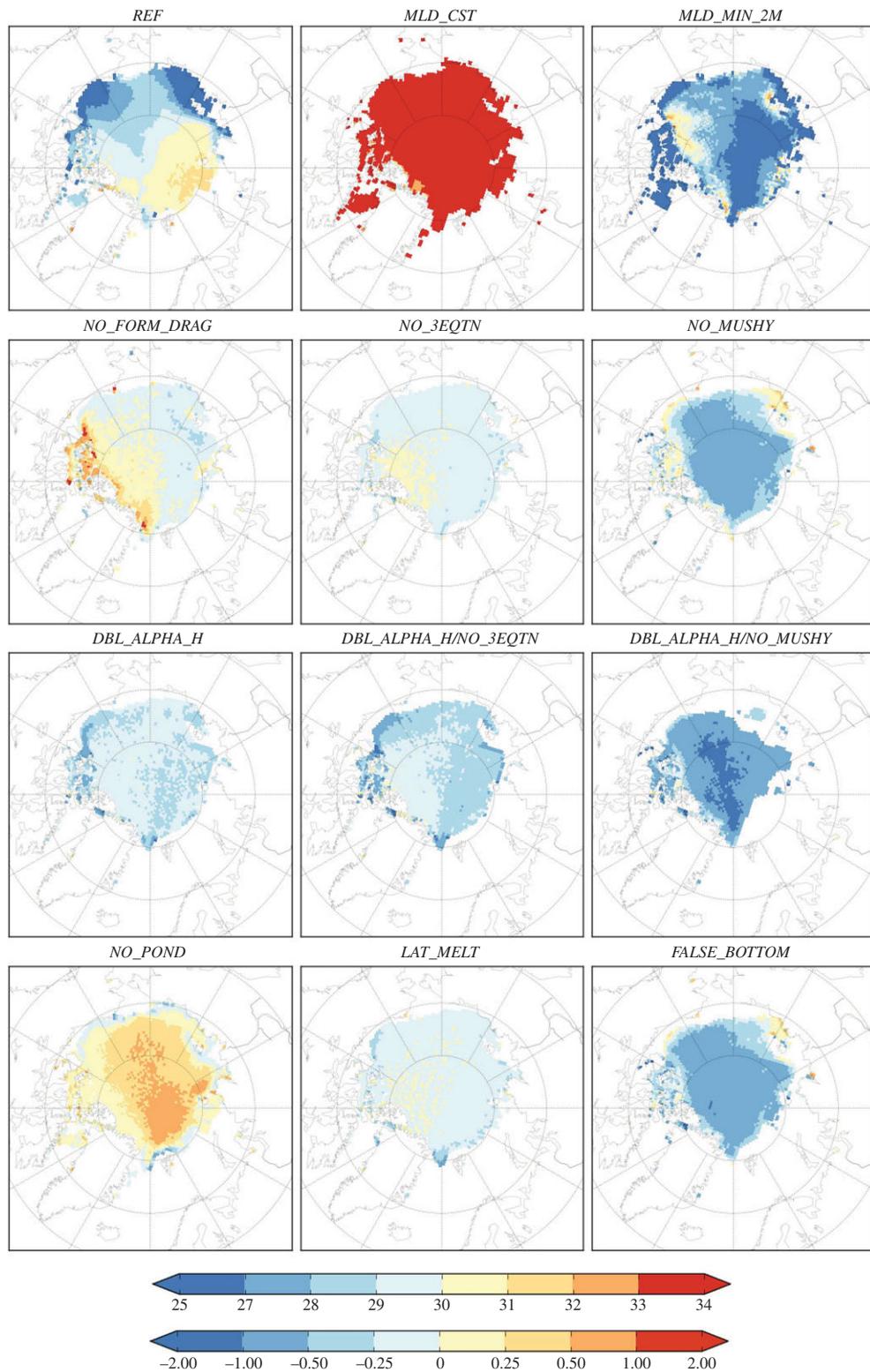
Figure 11. August ML salinity climatology maps over the period 1994–2013 for all sensitivity runs. Note that the map for the *REF* model run is given in absolute salinity values (PSU, top colour bar), while all other model runs are given as difference in salinity with respect to *REF* (PSU, bottom colour bar). (Online version in colour.)

and oceanic heat exchange coefficients in the former (later) regions when the form drag is accounted for.

Switching off the melt ponds in *NO_POND* results, as expected, in a large increase in the concentration and volume of ice throughout the summer season, due to a lowering of the incoming solar radiation, F_s. In August, for example, the patterns are similar, albeit more intense, to *MLD_CST* with a large increase of A and decrease of T_{mix} over most of the eastern portion of the Arctic Ocean and a more homogeneous increase of S_{mix} and H. Interestingly, *FALSE_BOTTOM* performs very much like *NO_MUSHY* (and less like *DBL_ALPHA_H / NO_MUSHY*), indicating that reducing the bottom heat flux whenever melt ponds are prevalent could play an important role in accurately simulating the total mass balance of the Arctic sea ice cover.

Introducing the new lateral melt parametrization in *LAT_MELT* results in a significant decrease of concentration ($\Delta A \sim -7.5\%$) and thickness ($\Delta H \sim -20\,\mathrm{cm}$) in the marginal ice zone, but without notable changes of the ML salinity and temperature.

(c) Impact on the main sea ice characteristics

We now assess the main sea ice characteristics from the various model simulations over the entire Arctic basin. This provides a simple overview of the sea ice response to prescribed atmospheric and oceanic forcing. In figure 12, we look at the impact of the new model physics on the total ice area (figure 12*a–c*), total ice extent (figure 12*d–f*) and total ice volume (figure 12*g–i*). To distinguish between the different model responses shown in figure 12, we present in figures 13*a–c* and 14*a–c* a series of scatter plots showing the average and trend in sea ice area (SIA), SIE, defined as the total area covered by ice with a concentration higher than 15% and SIV over the period 1993–2010 in August and September (note that we use the same colour scheme as in figure 12). The slightly shorter time period chosen reflects the time span of the *SST_TIME* simulation that is limited by the MYO reanalysis data used. Note that the results shown on figures 13 and 14 are similar over the period 1993–2013.

In order to assess the inter-annual variability of the model simulations, we also calculate the correlation and de-trended correlation between each model run annual time-series (SIA, SIE and SIV) and the corresponding observational dataset. Figures 13*d–f* and 14*d–f* show these results in a scatter plot format, respectively, in August and September. Note that we choose to compare the SIA and SIE results to the Bootstrap processing of passive microwave data [61]. While absolute values between NASA Team and Bootstrap sea ice concentration vary considerably in the summer, the detrended time series are similar. For comparison purposes, we also show a point corresponding to the Schröder *et al.* [57] model set-up that we refer to as *SFFT14*.

Figures 13 and 14 reveal that the physical processes tested in this study introduce a wide spread in the main sea ice characteristics in both the mean and the trend. In September, the average SIA ranges from $3.1 \times 10^6\,\mathrm{km}^2$ (*NO_MUSHY*) to $5.1 \times 10^6\,\mathrm{km}^2$ (*SST_TIME*), the average SIE from $4.5 \times 10^6\,\mathrm{km}^2$ (*DBL_ALPHA_H / NO_MUSHY*) to $6.2 \times 10^6\,\mathrm{km}^2$ (*SST_TIME*) and the average SIV from $4.0 \times 10^6\,\mathrm{km}^2$ (*DBL_ALPHA_H / NO_MUSHY*) to $12.7 \times 10^6\,\mathrm{km}^2$ (*SST_TIME*). The September SIA trend ranges from $-1700 \times 10^6\,\mathrm{km}^2\,\mathrm{decade}^{-1}$ (*SST_TIME*) to $-750 \times 10^6\,\mathrm{km}^2\,\mathrm{decade}^{-1}$ (*NO_POND*), the SIE trend ranges from $-1400 \times 10^6\,\mathrm{km}^2\,\mathrm{decade}^{-1}$ (*SFFT14*) to $-620 \times 10^6\,\mathrm{km}^2\,\mathrm{decade}^{-1}$ (*MLD_CST*), and the SIV trend ranges from $-3.9 \times 10^{12}\,\mathrm{m}^3$ (*SST_TIME*) to $-1.6 \times 10^{12}\,\mathrm{m}^3\,\mathrm{decade}^{-1}$ (*DBL_ALPHA_H / NO_MUSHY*).

Looking in more detail at the individual runs in figures 13*a–c* and 14*a–c*, we see that the average SIA, SIE and SIV (to a lesser degree) of most model simulations are larger than for the *SFFT14* simulation of Schröder *et al.* [57] and closer to the passive microwave observations (not closer to PIOMAS). The only simulations that have similar SIA and SIE (but lower SIV) to the *SFFT14* run are *NO_MUSHY* and *DBL_ALPHA_H / NO_MUSHY* that use the same thermodynamic treatment of the ice Bitz & Lipscomb [36] and the same parametrization of the flushing of melt ponds [38] as is used in Schröder *et al.* [57]. Two outlier runs on figure 12, *NO_MUSHY* (and *DBL_ALPHA_H/ NO_MUSHY* not shown) and *SST_TIME* (and to a lesser degree *NO_POND*) show a very low
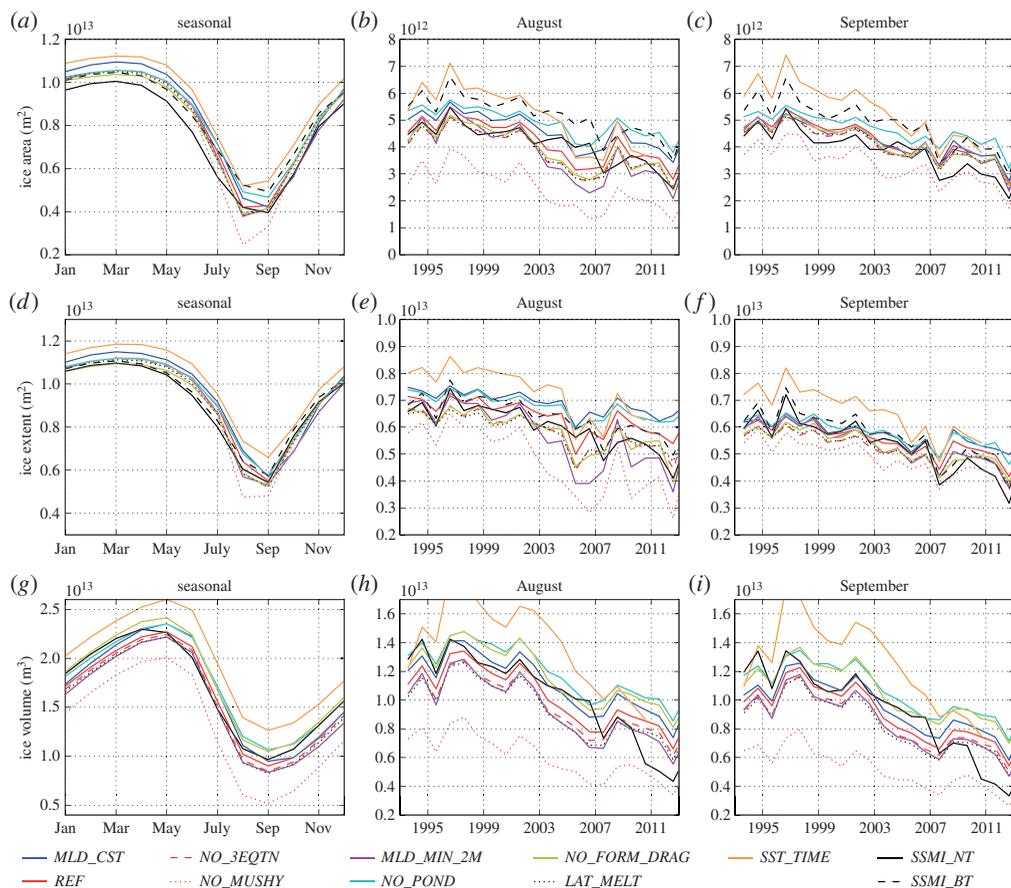
Figure 12. Impact of the sensitivity model runs on the total area (*a–c*), total extent (*d–f*) and total volume (*g–i*) of sea ice. Figures on the first column show the seasonal climatology calculated over the period 1993–2012, while columns two and three show the time series for August and September. The colour code is a follows: *REF* in red, *MLD_CST* in blue, *SST_TIME* in green, *MLD_MIN_2M* in mauve, *SSMI_NT* and *PIOMAS* in solid black and *SSMI_BT* in dashed black. (Online version in colour.)

and high total volume of ice throughout the season (figure 12*g–i*). In *SST_TIME*, we use a time-dependent SST from the MYO reanalysis which is equivalent to modifying the oceanic flux F_{adv} shown on figure 1. As clearly demonstrated in Turner & Hunke [38], by introducing a new mushy layer thermodynamic scheme [37] (*NO_3EQTN* and *REF*), we also modify the flushing parametrization used in the earlier set-up of CICE [36] (*NO_MUSHY*). This results in less melt pond water being flushed in the summer in *NO_MUSHY* as opposed to in *NO_3EQTN* (or *REF*) which lowers the albedo and increases the incoming shortwave radiation penetrating the sea ice and ML system, resulting in a strong reduction in SIV as shown in figure 12*g–i*. This is also highlighted by the additional ice surface heat flux F_s, in *REF* compared with *NO_MUSHY*. Inversely, in *NO_POND* where the thickness and area of the melt ponds are set artificially to zero, the surface heat flux, F_s, is reduced, resulting in less ice melt and a slower ice edge retreat (figures 12, 13 and 14).

Observed differences in the mean sea ice characteristics between the various model simulations can also be related to a shift in their seasonal responses. As highlighted in figure 12, introducing a prognostic ML results in an overall depletion of ice across the Arctic (in both thickness and concentration). From figure 12*g* (but also *a* and *d*), we see that from January to May, the sea ice in the reference run *REF* grows slower than in *MLD_CST*. We attribute this to the entrainment of warm water from the deeper ocean as the ML deepens from about 30 m in January
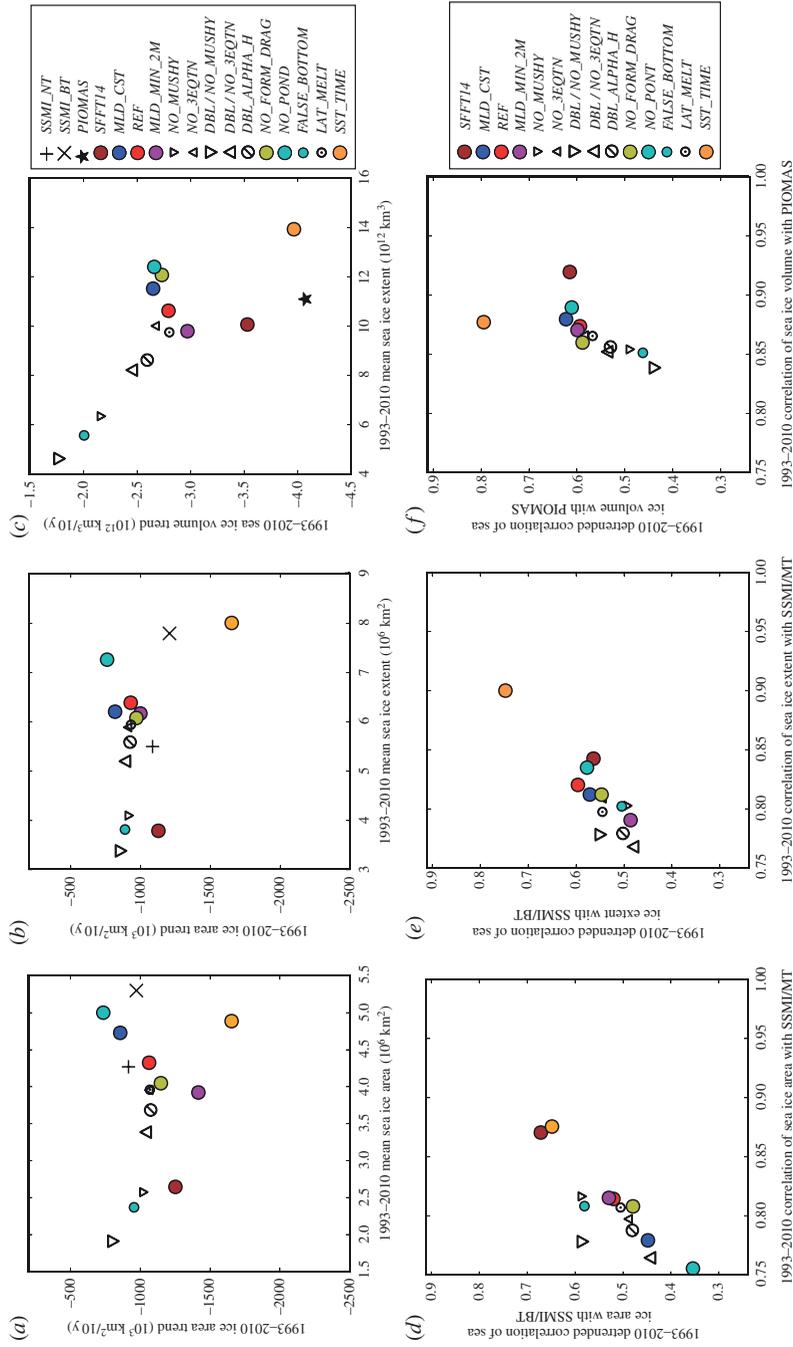
Figure 13. Scatter plots of the trends versus averages over the period 1993–2010 of the August total SIA (*a*), SIE (*b*) and SIV (*c*). Scatter plots of the full and de-trended correlation coefficients between the model and observed time series of the total SIA (*d*), SIE (*d*) and SIV (*f*). Here we correlate model SIA and extent with the SSMI_BT observation and model volume with PIOMAS. We show 13 model runs described in §2. As a reference we also show values from the model run discussed in Schröder *et al.* [57]. (Online version in colour.)

24

rsta.royalsocietypublishing.org   Phil. Trans. R. Soc. A **373**: 20140167
....

Figure 14. Scatter plots of the trends versus averages over the period 1993–2010 of the September total SIA (*a*), SIE (*b*) and SIV (*c*). Scatter plots of the full and de-trended correlation coefficients between the model and observed time series of the total SIA (*d*), SIE (*e*) and SIV (*f*). Here we correlate model SIA and extent with the *SSMI_BT* observation and model volume with *PIOMAS*. We show 13 model runs described in §2. As a reference we also show values from the model run discussed in Schröder *et al.* [57]. (Online version in colour.)
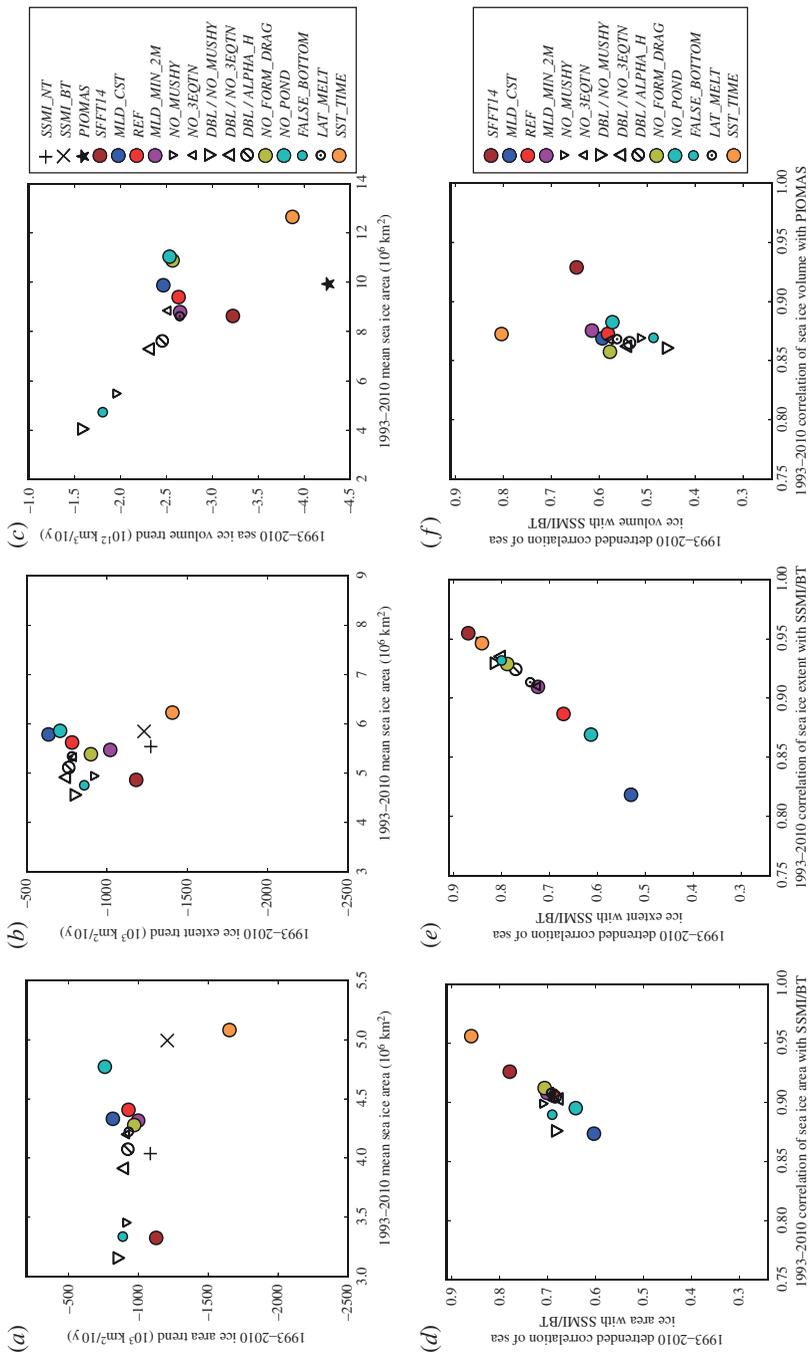
to about 50 m in May, resulting in a large positive bottom flux F_{bot} (figure 2) that is not present in the *MLD_CST* run. Looking at the mean ice growth and melt contributions in figure 4 and for individual months shows that the difference is due to less frazil ice formation in *REF* between January and May as discussed in §3a.

As expected, the trends in SIV correlate with the mean SIV (figures 13*c* and 14*c*). For example, the ice-covered area ice in August in *SST_TIME* is almost double that of *NO_MUSHY* and melting sea ice at the same volume per decade in both runs would require a significant increase in the local melt rates that has no physical justification. Hence, the SIV trend is more than halved in *NO_MUSHY* (-1.7×10^{12} m^3 decade^{-1} in September) in comparison to *SST_TIME* (-4×10^{12} m^3 decade^{-1} in September) as shown in figure 14*c*.

We turn now to the scatter plot correlations presented in figures 13*d–f* and 14*d–f*. In the following discussion, we denote R the correlation and $R^{\star}$ the detrended correlation. Figure 13*d–f* shows that apart from *SFFT14* and *SST_TIME*, all other runs perform relatively poorly in reproducing the observed variability in the August SIA ($R \leq 0.75$ and $R^{\star} \leq 0.45$) and only slightly better for the SIE ($R \leq 0.85$ and $R^{\star} \leq 0.6$) and SIV ($R \leq 0.88$ and $R^{\star} \leq 0.63$). The September correlations (figure 14*d–f*) are higher in all simulations for SIA ($0.86 \leq R \leq 0.95$ and $0.6 \leq R^{\star} \leq 0.86$) and SIE ($0.82 \leq R \leq 0.95$ and $0.53 \leq R^{\star} \leq 0.86$) and similar for SIV ($0.86 \leq R \leq 0.92$ and $0.45 \leq R^{\star} \leq 0.8$). The *SFFT14* and *SST_TIME* runs still perform best across all characteristics but note that *NO_MUSHY*, *DBL_ALPHA_H / NO_MUSHY*, *DBL_ALPHA_H / NO_3EQTN*, FD/OFF and *DBL_ALPHA_H* also perform well (in decreasing order) in representing the observed inter-annual variability of the SIE.

Summarizing figures 12, 13 and 14, one can conclude that introducing the new physical parametrizations schemes described in §2 and, in particular, the new mushy-layer thermodynamic approach of Turner *et al.* [37] can improve the main basin average characteristics of the sea ice with respect to the *SFFT14* set-up. The improvement is particularly clear for the August SIA and SIE and the September SIA. However, the potential improvement in simulating the sea ice trends is not so clear, where we see an improvement in the August SIE trend but a deterioration of the SIV trends. The inter-annual variability of the main sea ice characteristics quantified by the correlation coefficients, R and $R^{\star}$, figures 13 and 14 show that the model simulations (with the exception of *SST*) do not perform as well as the *SFFT14* simulation. To understand these differences, one must realize that inter-annual variability is dependent on the mean state of the ice pack. We expect, for example, a thinner and less concentrated sea ice cover to be more responsive to inter-annual variability in the external forcing. This highlights the fact that even within a stand-alone set-up, tuning a sea ice model to reproduce simultaneously the mean, trends and inter-annual variability of the main sea ice characteristics is a delicate exercise. Interestingly, we find that the *SST_TIME* simulation outperforms all other model runs in almost every single category both in terms of averages and correlations (note that the *SFFT14* run is better at capturing September SIE inter-annual variability). While this result is unsurprising in the sense that a time-dependent SST from reanalysis captures a large part of the inter-annual variability of the atmospheric and oceanic forcing as well as of the SIE, it nevertheless highlights once more the importance of the upper ocean in driving the sea ice response and the coupled nature of the sea ice–ML system [16,62].

4. Discussion and conclusion

We have presented a stand-alone sea ice model sensitivity study focusing on the processes controlling the summer melt of Arctic sea ice. In addition to the parametrization schemes already implemented in the state of the art Los Alamos community sea ice model CICE, v. 5.0.2 (e.g. explicit melt ponds, a form drag parametrization and a halodynamic brine drainage scheme), we implement in the model and test three new schemes: (i) a prognostic ML model; (ii) a three equation boundary condition; and (iii) a parametrization of lateral melting explicitly accounting for the average floe size and floe size distribution dependence. For each simulation, the total melt is decomposed into its surface, bottom and lateral melt components. While our

modelling approach is limited in that the sea ice model is not coupled to an atmosphere or ocean model preventing a complete representation of feedback processes, it has the advantage that it disentangles model physics uncertainty from the internal variability inherent to a fully coupled model. The reference simulation of this stand-alone sea ice–ML model was still able to simulate accurately the mean state, trends and inter-annual variability of the main Arctic sea ice cover characteristics (ice area, extent and volume).

Our sensitivity study demonstrates that the various sea ice parametrization schemes have the potential to significantly impact the sea ice and ML characteristics on regional and basin scales. Introducing a prognostic ML resulted in an overall decrease of sea ice across the Arctic (in both thickness and concentration). In this simulation, ice growth is reduced due to entrainment of warm water from the deeper ocean as the ML deepens from December to May, while ice growth is enhanced in Autumn due to a more rapid cooling of the shallow ML. Switching off the form drag parametrization increased ice thickness ($\sim +1\,\mathrm{m}$) over the heavily ridged regions north of Greenland and the Canadian Archipelago and reduced ice thickness ($\sim -0.25\,\mathrm{m}$) over the Russian continental shelves. We attribute this to the decreased (increased) surface and bottom melt in the former (latter) regions, due to the increased momentum and heat transfer coefficients in these deformed (undeformed) areas. The impact of the three equation boundary conditions was localized in the marginal ice zone and acts exclusively during summer, when the temperature difference between the ML and the IO interface that drives the bottom melt is reduced. The halodynamic brine drainage scheme resulted in a strong reduction in ice thickness (more than or equal to $1\,\mathrm{m}$), due to reduced flushing of melt ponds which lowers the surface albedo and thus results in additional absorption of solar radiation, increasing surface and bottom melt. Conversely, switching off the explicit melt pond scheme resulted in a large increase in sea ice thickness and concentration. Introducing the new parametrization of lateral melt resulted in a large increase in lateral melt over the ice edge that is accompanied by a reduction in bottom melt. Across all simulations, we find that bottom melt accounts typically for around two-thirds of the total melt, surface melt accounts for nearly one-third and lateral melt accounts for less than 10%.

Quantitative optimization of the simulated sea ice and ML against observations was not the primary goal of this study and is a topic that will be pursued in future work in stand-alone and IO-coupled simulations. Nevertheless, this study reveals that such optimization is complex and will likely require a trade-off between accurately simulating the mean ice state characteristics and capturing the inter-annual ice state variability. The sensitivity of the inter-annual variability to different sea ice physics parametrization schemes, alludes to the importance of accurate sea ice physics representation in climate models, especially when seeking skillfull seasonal sea ice forecasts. In particular, the difficulty in current sea ice models to reproduce and forecast years with anomalously high or low SIE [63] is likely to be due to deficiencies in the physical representation of sea ice in these models. Moreover, the wide spread in the simulated mean state and trend of the main sea ice characteristics in our sensitivity study indicates that model physics uncertainty could dominate overall sea ice uncertainty in general circulation models [64].

Appendix A. Impact of floe size distribution on lateral melt

(a) Some preliminary equations and definitions

Defining $n_r(r)\,\mathrm{d}r$ as the area fraction covered by ice of size r, one has the number of floes of size r per unit area as $n_r(r)/\pi r^2$. To express $n_r(r)$ as a function of the floe area distribution $n_s(s)$ with

$s = \pi r^2$, we need the identity:

$$n_s(s) = \frac{n_r(\sqrt{s/\pi})}{2\pi\sqrt{s/\pi}} \tag{A 1}$$

From now on, we use the simplified notation $n(r)$ instead of $n_r(r)$. We have the condition of normalization for $n(r)$:

$$\int_0^\infty n(r)\,dr = 1 \tag{A 2}$$

For a total surface of ice A, we can express the first average floe size $\bar{r}_1$ as:

$$\bar{r} = \int_0^\infty A\frac{n(r)}{\pi r^2}r\,dr \Big/ \int_0^\infty S\frac{n(r)}{\pi r^2}\,dr. \tag{A 3}$$

Note that $\int_0^\infty A(n(r)/\pi r^2)\,dr$ is the total number of floes in that area S. Let us choose two function $n(r)$, one for a fixed floe size case ($n_1(r)$) and one for a power law FSD ($n_2(r)$). We also assume that both have the same average floe size $\bar{r}$. For the fixed floe size case, the normalization equation (A 2) is satisfied for $n_1(r) = \delta(r - \bar{r})$. The normalization equation for $n_2(r)$ gives

$$\int_0^\infty n_2(r)\,dr = \int_0^\infty Cr^{-\zeta}\,dr = \int_{r_{min}}^\infty Cr^{-\zeta}\,dr = C\frac{r_{min}^{-\zeta+1}}{\zeta-1} = 1. \tag{A 4}$$

Therefore, one can write

$$n_2(r) = (\zeta - 1)r^{-\zeta}r_{min}^{\zeta-1}. \tag{A 5}$$

Now the condition (A 3) can be written as

$$\int_0^\infty A\frac{n_2(r)}{\pi r^2}r\,dr \Big/ \int_0^\infty A\frac{n_2(r)}{\pi r^2}\,dr = \int_0^\infty r^{-\zeta-1} \Big/ \int_0^\infty r^{-\zeta-2} = \frac{\zeta+1}{\zeta}r_{min} = \bar{r}. \tag{A 6}$$

And we can write r_{min} as a function of $\bar{r}$.

(b) On why power law FSD melt less ice laterally than fixed floe size

We know that the rate of lateral melting of the total ice area is proportional to the total perimeter P of the floes:

$$\frac{\partial A}{\partial t} = -mP = -m\frac{P}{A}A, \tag{A 7}$$

where m is the lateral rate of melt (in $\mathrm{cm\,s^{-1}}$). Let us calculate this perimeter for the two situations described above. Note both have the same average floe size $\bar{r}$. We have

$$P_1 = 2A\frac{1}{\bar{r}} \tag{A 8}$$

and

$$P_2 = A\int_0^\infty \frac{n_2(r)}{\pi r^2}2\pi r\,dr = 2A\frac{(\zeta-1)(\zeta+1)}{\zeta^2}\frac{1}{\bar{r}} = 2P_0(\zeta)A\frac{1}{\bar{r}}. \tag{A 9}$$

Typical observed values of ζ are in the range 0 to 2. But the total area of ice diverges if $\zeta < 1$ and one needs to introduce a upper floe size cut-off value. Example values in this range for the function P_0 are $P_0(2.0) = 0.75$, $P_0(1.75) = 0.67$, $P_0(1.5) = 0.56$, $P_0(1.25) = 0.36$, $P_0(1.1) = 0.17$ and $P_0(1.0) = 0$. Herman [51] introduces a different function P_0 that takes the values $P_0(2.0) = 1$, $P_0(1.75) = 0.86$, $P_0(1.5) = 0.67$, $P_0(1.25) = 0.4$, $P_0(1.1) = 0.18$ and $P_0(1.0+) = 0$.

References

1. Stroeve JC, Kattsov V, Barrett A, Serreze M, Pavlova T, Holland M, N.Meier W. 2012 Trends in Arctic sea ice extent from CMIP5, CMIP3 and observations. *Geophys. Res. Lett.* **39**, L16502. (doi:10.1029/2012GL052676)
2. Kwok R, Rothrock DA. 2009 Decline in Arctic sea ice thickness from submarine and ICES at records: 1958–2008. *Geophys. Res. Lett.* **36**, L15501. (doi:10.1029/2009GL039035)

28

rsta.royalsocietypublishing.org *Phil. Trans. R. Soc. A* **373**: 2014016

3. Laxon SW *et al.* 2013 CryoSat-2 estimates of Arctic sea ice thickness and volume. *Geophys. Res. Lett.* **40**, 732–737. (doi:10.1002/grl.50193)

4. Lindsay R, Schweiger A. 2013 Arctic sea ice thickness loss determined using subsurface, aircraft, and satellite observations. *Cryosphere* **9**, 269–283. (doi:10.5194/tc-9-269-2015)

5. Comiso JC. 2011 Large decadal decline of the arctic multiyear ice cover. *J. Clim.* **25**, 1176–1193. (doi:10.1175/JCLI-D-11-00113.1)

6. Rampal P, Weiss J, Marsan D, Bourgoin M. 2009 Arctic sea ice velocity field: general circulation and turbulent-like fluctuations. *J. Geophys. Res.* **114**, C10014. (doi:10.1029/2008JC005227)

7. Spreen G, Kwok R, Menemenlis D. 2011 Trends in Arctic sea ice drift and role of wind forcing: 1992–2009. *Geophys. Res. Lett.* **38**, L19501. (doi:10.1029/2011GL048970)

8. Rampal P, Weiss J, Dubois C, Campin J-M. 2011 Ipcc climate models do not capture arctic sea ice drift acceleration: consequences in terms of projected sea ice thinning and decline. *J. Geophys. Res.* **116**, C00D07. (doi:10.1029/2011JC007110)

9. Notz D. 2012 Challenges in simulating sea ice in earth system models. *WIREs Clim. Change* **3**, 509–526. (doi:10.1002/wcc.189)

10. Feltham DL, Untersteiner N, Wettlaufer JS, Worster MG. 2006 Sea ice is a mushy layer. *Geophys. Res. Lett.* **40**, 91–112.

11. McPhee MG. 2012 Advances in understanding ice–ocean stress during and since AIDJEX. *Cold Regions Sci. Technol.* **76**, 24–36. (doi:10.1016/j.coldregions.2011.05.001)

12. Coon M, Kwok R, Levy G, Pruis M, Schreyer H, Sulsky D. 2007 Arctic ice dynamics joint experiment (AIDJEX) assumptions revisited and found inadequate. *J. Geophys. Res. Oceans* **112**, C11S90. (doi:10.1029/2005JC003393)

13. Feltham DL. 2008 Sea ice rheology. *Annu. Rev. Fluid Mech.* **40**, 91–112. (doi:10.1146/annurev.fluid.40.111406.102151)

14. Richter-Menge JA, Perovich DK, Dubois C, Elder BC, Claffey K, Rigor I, Ortmeyer M. 2011 Ice mass-balance buoys: a tool for measuring and attributing changes in the thickness of the Arctic sea-ice cover. *Ann. Glaciol.* **44**, 205–210. (doi:10.3189/172756406781811727)

15. Toole JM, Krishfield RA, Timmermans M-L, Proshutinsky A. 2011 The ice-tethered profiler: argo of the Arctic. *Oceanography* **24**, 126–135. (doi:10.5670/oceanog.2011.64)

16. Perovich D, Richter-Menge J, Polashenski C, Elder B, Arbetter T, Brennick O. 2014 Sea ice mass balance observations from the north pole environmental observatory. *Geophys. Res. Lett.* **41**, 2014GL059356. (doi:10.1002/2014GL059356)

17. Steele M. 1992 Sea ice melting and floe geometry in a simple ice–ocean model. *J. Geophys. Res.* **97**, 17 729–17 738. (doi:10.1029/92JC01755)

18. Strong C, Rigor IG. 2013 Arctic marginal ice zone trending wider in summer and narrower in winter. *Geophys. Res. Lett.* **40**, 4864–4868. (doi:10.1002/grl.50928)

19. Ebert EE, Curry JA. 1993 An intermediate one-dimensional thermodynamic sea ice model for investigating ice-atmosphere interactions. *J. Geophys. Res.* **98**, 10 085–10 109. (doi:10.1029/93JC00656)

20. Petty AA, Feltham DL, Holland PR. 2012 Impact of atmospheric forcing on antarctic continental shelf water masses. *J. Phys. Oceanogr.* **43**, 920–940. (doi:10.1175/JPO-D-12-0172.1)

21. Johnson M, Gaffigan S, Hunke E, Gerdes R. 2007 A comparison of arctic ocean sea ice concentration among the coordinated aomip model experiments. *J. Geophys. Res. Oceans* **112**, C04S11. (doi:10.1029/2006JC003690)

22. Maslowski W, Clement Kinney J, Higgins M, Roberts A. 2012 The future of arctic sea ice. *Annu. Rev. Earth Planet. Sci.* **40**, 625–654. (doi:10.1146/annurev-earth-042711-105345)

23. Keen AB, Hewitt HT, Ridley JK. 2013 A case study of a modelled episode of low Arctic sea ice. *Clim. Dyn.* **41**, 1229–1244. (doi:10.1007/s00382-013-1679-y)

24. Rae JGL, Hewitt HT, Keen AB, Ridley JK, Edwards JM, Harris CM. 2014 A sensitivity study of the sea ice simulation in the global coupled climate model, HadGEM3. *Ocean Modell.* **74**, 60–76. (doi:10.1016/j.ocemod.2013.12.003)

25. Hibler W, Hutchings J, Ip C. 2006 Sea-ice arching and multiple flow states of arctic pack ice. *Ann. Glaciol.* **44**, 339–344. (doi:10.3189/172756406781811448)

26. Petty AA, Holland PR, Feltham DL. 2014 Sea ice and the ocean mixed layer over the antarctic shelf seas. *Cryosphere* **8**, 761–783. (doi:10.5194/tc-8-761-2014)

27. Flocco D, Schroeder D, Feltham DL, Hunke EC. 2012 Impact of melt ponds on arctic sea ice simulations from 1990 to 2007. *J. Geophys. Res.* **117**, C09032. (doi:10.1029/2012JC008195)

28. Hunke EC, Lipscomb WH, Turner AK, Jeffery N, Elliott S. 2013 CICE: the Los Alamos Sea Ice Model Documentation and Software User's Manual v. 5.0.

29. Lipscomb W, Hunke E, Maslowski W, Jakacki J. 2007 Ridging, strength, and stability in high-resolution sea ice models. *J. Geophys. Res* **112**, C03S91. (doi:10.1029/2005JC003355)

30. Lipscomb W, Hunke E. 2004 Modeling sea ice transport using incremental remapping. *Mon. Weather Rev.* **132**, 1341–1354. (doi:10.1175/1520-0493(2004)132<1341:MSITUI>2.0.CO;2)

31. Tsamados M, Feltham DL, Wilchinsky AV. 2013 Impact of a new anisotropic rheology on simulations of arctic sea ice. *J. Geophys. Res. Oceans* **118**, 91–107. (doi:10.1029/2012JC007990)

32. Hunke E, Dukowicz J. 2002 The elastic-viscous-plastic sea ice dynamics model in general orthogonal curvilinear coordinates on a sphere - incorporation of metric terms. *Mon. Weather Rev.* **130**, 1848–1865. (doi:10.1175/1520-0493(2002)130<1848:TEVPSI>2.0.CO;2)

33. Rothrock D. 1975 The energetics of the plastic deformation of pack ice by ridging. *J. Geophys. Res. Oceans* **80**, 4514–4519. (doi:10.1029/JC080i033p04514)

34. Hunke EC, Hebert DA, Lecomte O. 2013 Level-ice melt ponds in the Los Alamos sea ice model, CICE. *Ocean Modell.* **71**, 26–42. (doi:10.1016/j.ocemod.2012.11.008)

35. Briegleb B, Light B. 2007 A delta-eddington multiple scattering parameterization for solar radiation in the sea ice component of the community climate system model. ncar tech. Technical report, Note NCAR/TN-472+ STR, National Center for Atmospheric Research, 2007.

36. Bitz C, Lipscomb W. 1999 An energy-conserving thermodynamic model of sea ice. *J. Geophys. Res.* **104**, 15 669–15 677. (doi:10.1029/1999JC900100)

37. Turner AK, Hunke EC, Bitz CM. 2013 Two modes of sea-ice gravity drainage: a parameterization for large-scale modeling. *J. Geophys. Res. Oceans* **118**, 2279–2294. (doi:10.1002/jgrc.20171)

38. Turner AK, Hunke E. 2015 Impacts of a mushy-layer thermodynamic approach in global sea-ice simulations using the CICE sea-ice model. *J. Geophys. Res. Oceans* **120**, 1253–1275. (doi:10.1002/2014JC010358)

39. Maykut GA, McPhee MG. 1995 Solar heating of the arctic mixed layer. *J. Geophys. Res.* **100**, 24 691–24 703. (doi:10.1029/95JC02554)

40. Tsamados M, Feltham DL, Schroeder D, Flocco D, Farrell SL, Kurtz N, Laxon SW, Bacon S. 2014 Impact of variable atmospheric and oceanic form drag on simulations of arctic sea ice. *J. Phys. Oceanogr.* **44**, 1329–1353. (doi:10.1175/JPO-D-13-0215.1)

41. Lu P, Li Z, Cheng B, Leppäranta M. 2011 A parameterization of the ice–ocean drag coefficient. *J. Geophys. Res.* **116**, C07019. (doi:10.1029/2010JC006878)

42. Lüpkes C, Gryanik VM, Hartmann J, Andreas EL. 2012 A parametrization, based on sea ice morphology, of the neutral atmospheric drag coefficients for weather prediction and climate models. *J. Geophys. Res.* **117**, D13112. (doi:10.1029/2012JD017630)

43. Hunke EC. 2014 Weighing the importance of surface forcing on sea ice: a september 2007 modeling study. *Q. J. R. Meteorol. Soc.* (doi:10.1002/qj.2353)

44. Schröder D, Vihma T, Kerber A, Brümmer B. 2003 On the parameterization of turbulent surface fluxes over heterogeneous sea ice surfaces. *J. Geophys. Res.* **108**, 3195. (doi:10.1029/2002JC001385)

45. Maykut GA, Perovich DK. 1987 The role of shortwave radiation in the summer decay of a sea ice cover. *J. Geophys. Res.* **92**, 7032–7044. (doi:10.1029/JC092iC07p07032)

46. Perovich DK. 1983 On the summer decay of a sea ice cover. PhD thesis, University of Washington, Seattle, WA, USA.

47. Kraus EB, Turner JS. 1967 A one-dimensional model of the seasonal thermocline ii. the general theory and its consequences. *Tellus* **19**, 98–106. (doi:10.1111/j.2153-3490.1967.tb01462.x)

48. Ferry N, Masina S, Storto A, Haines K, Valdivieso M, Barnier B, Molines J-M. 2011 Product user manual global-reanalysis-phys-001-004-a and b, myocean. Technical report.

49. Steele M, Zhang J, Ermold W. 2010 Mechanisms of summertime upper arctic ocean warming and the effect on sea ice melt. *J. Geophys. Res.* **115**, C11004. (doi:10.1029/2009JC005849)

50. Bitz CM, Gent PR, Woodgate RA, Holland MM, Lindsay R. 2006 The influence of sea ice on ocean heat uptake in response to increasing CO_2. *J. Clim.* **19**, 2437–2450. (doi:10.1175/JCLI3756.1)

51. Herman A. 2010 Sea-ice floe-size distribution in the context of spontaneous scaling emergence in stochastic systems. *Phys. Rev. E* **81**, 066123. (doi:10.1103/PhysRevE.81.066123)

52. Weiss J, Marsan D. 2004 Scale properties of sea ice deformation and fracturing. *C. R. Phys.* **5**, 735–751. (doi:10.1016/j.crhy.2004.09.005)

53. Steele M, Morison JH, Untersteiner N. 1989 The partition of air–ice–ocean momentum exchange as a function of ice concentration, roe size, and draft. *J. Geophys. Res.* **94**, 12 739–12 750. (doi:10.1029/JC094iC09p12739)

54. Schmidt GA, Bitz CM, Mikolajewicz U, Tremblay L-B. 2004 Ice–ocean boundary conditions for coupled models. *Ocean Modell.* **7**, 59–74. (doi:10.1016/S1463-5003(03)00030-1)

55. Notz D. 2005 Thermodynamic and fluid-dynamical processes in sea ice. PhD thesis, University of Cambridge.

56. McPhee MG. 2008 Physics of early summer ice/ocean exchanges in the western weddell sea during ispol. *Deep Sea Res. II Top. Stud. Oceanogr.* **55**, 1075–1097. (doi:10.1016/j. dsr2.2007.12.022)

57. Schröder D, Feltham DL, Flocco D, Tsamados M. 2014 September arctic sea-ice minimum predicted by spring melt-pond fraction. *Nat. Clim. Change* **4**, 353–357. (doi:10.1038/ nclimate2203)

58. Notz D. 2013 Sea-ice extent provides a limited metric of model performance. *Cryosphere* **7**, 3095–3131. (doi:10.5194/tcd-7-3095-2013)

59. Kanamitsu M, Ebisuzaki W, Woollen J, Yang S, Hnilo JJ, Fiorino M, Potter GL. 2002 NCEP-DOE AMIP-II Reanalysis (R-2). *Bull. Am. Meteorol. Soc.* **83**, 1631–1643. (doi:10.1175/ BAMS-83-11-1631)

60. Peralta-Ferriz C, Woodgate RA. 2014 Seasonal and interannual variability of pan-Arctic surface mixed layer properties from 1979 to 2012 from hydrographic data, and the dominance of stratification for multiyear mixed layer depth shoaling. *Prog. Oceanogr.* **134**, 19–53. (doi:10.1016/j.pocean.2014.12.005)

61. Comiso JC. 2000 updated 2014: Bootstrap sea ice concentrations from Nimbus-7 SMMR and DMSP SSM/I-SSMIS, v. 2 [1980–2013]. Boulder, CO: NASA DAAC at the National Snow and Ice Data Center.

62. Toole JM, Timmermans M-L, Perovich DK, Krishfield RA, Proshutinsky A, Richter-Menge J. 2010 Influences of the ocean surface mixed layer and thermohaline stratification on arctic sea ice in the central canada basin. *J. Geophys. Res. Oceans* **115**, C10018. (doi:10.1029/2009JC005660)

63. Stroeve J, Hamilton LC, Bitz CM, Blanchard-Wrigglesworth E. 2014 Predicting september sea ice ensemble skill of the search sea ice outlook 2008–2013. *Geophys. Res. Lett.* **41**, 2411–2418. (doi:10.1002/2014GL059388)

64. Massonnet F, Fichefet T, Goosse H, Bitz CM, Philippon-Berthier G, Holland MM, Barriat P-Y. 2012 Constraining projections of summer arctic sea ice. *Cryosphere Discuss.* **6**, 2931–2959. (doi:10.5194/tcd-6-2931-2012)

30

rsta.royalsocietypublishing.org *Phil. Trans. R. Soc. A* **373**: 20140167